Aircraft Navigation in GNSS-Denied Environments via Radio SLAM With Terrestrial Signals of Opportunity

Zaher M. Kassas, *Fellow, IEEE*, Nadim Khairallah, Joe J. Khalife, *Member, IEEE*, Chiawei Lee, Juan Jurado, *Member, IEEE*, Steven Wachtel, Jacob Duede, Zachary Hoeffner, Thomas Hulsey, Rachel Quirarte, and RunXuan Tay

***Abstract*— A radio simultaneous localization and mapping (radio SLAM) framework enabling aircraft navigation with terrestrial signals of opportunity (SOPs) is presented and experimentally validated. The framework does not assume availability of global navigation satellite system (GNSS) signals. Instead, it assumes the aircraft to have an initial estimate of its own states, after which it navigates by exploiting pseudorange measurements extracted from terrestrial SOPs, while estimating the states of the aircraft simultaneously with the SOPs' states. Two radio SLAM frameworks are presented: (i) tightly-coupled SOP-aided inertial navigation system (INS) and (ii) utilizing a Wiener process acceleration (WPA) dynamical model for the aircraft's dynamics instead of the INS. Results from four flight runs on a US Air Force C-12 aircraft, equipped with an altimeter and an industrial-grade inertial measurement unit (IMU), are presented. The flight runs took place over semi-urban (SU), urban (U), and rural (R) regions in California, USA; while exercising different aircraft maneuvers: holding (H), descending (D), and grid (G). Different *a priori* conditions of the SOPs' positions were studied: from all unknown, to some known, to all known. In all cases, the SOPs' clock error states (bias and drift) were unknown and estimated alongside the aircraft's states. The results consistently demonstrated the promise of real-world aircraft navigation via radio SLAM, yielding bounded errors along trajectories of tens of kilometers. The three-dimensional (3–D) position root-mean squared errors (RMSEs) are summarized next, where N denotes the number of SOPs exploited along the trajectory: (1) SU, H, INS-SOP, $N = 6$, 56.7 km in 8.5 minutes, maximum altitude of 5,577 ft: 43.27 m with all unknown and 10.14 m with all known; (2) U, H, INS-SOP, $N = 6$, 72.7 km in 12.9 minutes, maximum altitude of 5,906 ft: 89.82 m with all unknown and 16.97 m with all known; (3) SU, D, WPA-SOP, $N = 18$, 111.9 km in 20.0 minutes, maximum altitude of 6,234 ft: 36.42 m with all unknown and 18.62 m with all known; and (4) R, G, WPA-SOP, $N = 32$, 78.4 km in 13.8 minutes, maximum altitude of 7,546 ft: 67.01 m with all unknown and 25.65 m with all known.**

***Index Terms*— Aircraft, aerial vehicle, navigation, SLAM, radio SLAM, signals of opportunity, INS.**

I. Introduction

COMMUNICATIONS, navigation, and surveillance (CNS) technologies for civilian aviation as well as military operations are critically dependent on positioning, navigation, and timing (PNT) from global navigation satellite system (GNSS) [1]. Loss of GNSS jeopardizes safety-of-life applications, from precision approach and landing, to air traffic control (ATC), to collision avoidance [2], [3]. Such concerns are compounded as human are taken "out-of-the-loop" in applications such as beyond visual line of sight (BVLOS) unmanned aerial vehicle (UAV) [4] and urban air mobility (UAM) [5].

GNSS interference, whether intentional or unintentional, has been reported at an alarming rate over the past few years [6]. In 2021, according to the Global Aviation Data Management (GADM) of the International Air Transport Association (IATA), 586 GNSS jamming or suspected interference were reported in the Middle East and North Africa [7]. Globally, based on in-flight monitoring of aircraft GNSS receivers, the International Telecommunication Union (ITU) reported that more than 10,000 radio frequency interference (RFI) events were detected [8]. EUROCONTROL, a pan-European, civil-military organization dedicated to supporting European aviation, concluded that 38.5% of European en-route flight traffic operates through regions intermittently but regularly affected by GNSS RFI [9]. Two major RFI incidents were reported in the US in 2022. The first, lasting 33 hours, in which ATC warned pilots that GPS was unreliable within a 50-nautical-mile radius of the Denver International Airport, with RFI likely to be experienced by aircraft on the ground and as high as 40,000 feet above sea level [10]. The second, lasting 44 hours, which shut down a runway at Dallas-Fort

Manuscript received 28 July 2023; revised 6 February 2024 and 31 March 2024; accepted 11 May 2024. Date of publication 20 June 2024; date of current version 4 October 2024. This work was supported in part by the Office of Naval Research (ONR) under Grant N00014-19-1-2511, in part by the Air Force Office of Scientific Research (AFOSR) under Grant FA9550-22-1-0476, in part by the National Science Foundation (NSF) under Grant 2240512, in part by the U.S. Department of Transportation under Grant 69A3552047138 for the CARMEN University Transportation Center (UTC), and in part by the Laboratory Directed Research and Development program at Sandia National Laboratories. The Associate Editor for this article was S.-H. Kong. *(Corresponding author: Zaher M. Kassas.)*

Zaher M. Kassas is with the Department of Electrical and Computer Engineering, The Ohio State University, Columbus, OH 43210 USA (e-mail: zkassas@ieee.org).

Nadim Khairallah and Joe J. Khalife were with the Department of Mechanical and Aerospace Engineering, University of California, Irvine, CA 92697 USA.

Chiawei Lee, Juan Jurado, Steven Wachtel, Jacob Duede, Zachary Hoeffner, Thomas Hulsey, and Rachel Quirarte are with the Test Pilot School, U.S. Air Force, Edwards Air Force Base, Edwards, CA 93524 USA.

RunXuan Tay is with the Republic of Singapore Air Force, Singapore 534236.

Digital Object Identifier 10.1109/TITS.2024.3405908

Worth International Airport after aviation authorities said GPS signals there aren't reliable, forcing approaching and departing aircraft to take cumbersome routes [11].

Several national and international regulatory bodies have put forth calls to find GNSS alternatives. In 2021, the National Institute of Standards and Technology (NIST) issued a report on "Foundational PNT Profile: Applying the Cybersecurity Framework for the Responsible Use of PNT Services," where it identified signals of opportunity (SOPs) and terrestrial radio frequency (RF) sources as a mitigation category that apply to the PNT profile [12]. In 2023, IATA invited the International Civil Aviation Organization (ICAO), in coordination with manufacturers and airspace user communities, to develop a global strategy on Alternative PNT to ensure continuity of flight and air traffic management (ATM) operations during interruptions of GNSS. IATA added that "on-board availability of alternative navigation capability using inertial navigation system (INS) / inertial reference unit (IRU) or other conventional radio navigation aids can be helpful" [13].

A. Navigation With SOPs

SOPs refer to ambient RF signals not intended as PNT sources [14], [15], e.g., AM/FM [16], [17], [18], digital television [19], [20], [21], cellular [22], [23], [24], and satellite communication signals [25], [26], [27]. Among terrestrial SOPs, cellular have shown tremendous promise as an alternative PNT source in GPS-jammed environments [28].

SOPs, particularly cellular, possess attractive attributes for aircraft navigation. First, in contrast to dead-reckoning-type sensors, absolute position information could be extracted from SOPs. Second, they are abundant in most locales of interest and their received carrier-to-noise ratio (C/N_0) is $20-30$ dBs higher than that of GNSS [29]. Third, they are cost-effective: the infrastructure is already deployed and retrofitting aircraft with SOP receivers is not as cumbersome as adding other sensors (e.g., cameras, lidar, radar, etc.). Fourth, radars and lidars are "proximity" sensors and are not particularly helpful at high altitudes due to lack of features and nearby objects. On the other hand, navigation with camera images coupled with feature and elevation maps would require additional terrain knowledge that might not be readily available onboard the aircraft. Plus, clouds below the aircraft would prevent cameras from getting any usable images from the ground. Finally, many SOPs are practically unaffected by dense smoke, fog, rain, snow, and other poor weather conditions.

Previous studies have shown that cellular SOPs could yield meter-level accuracy on ground vehicles [30], [31], [32] and sub-meter-level accuracy on low-altitude UAVs [33], [34], [35], [36]. All the aforementioned studies assumed that the cellular transmitters' positions are *known*.

When the SOP transmitters' positions are *unknown*, radio simultaneous localization and mapping (radio SLAM) was proposed. While there are several conceptualizations of radio SLAM [37], [38], [39], [40], [41], it is defined herein as the process whereby a navigating receiver (e.g., vehicle-mounted) estimates its own states (position, velocity, clock error, and potentially INS errors) simultaneously with the states of terrestrial SOPs (position and clock error) [42]. Radio SLAM observability was studied in [43], [44], and [45], motion planning for improved information gathering in [46] and [47], collaborative information fusion in [48] and [49], and demonstration of ground vehicle navigation in a GPS-jammed environment with a single SOP in [50].

B. Aircraft Navigation With SOPs

The potential of utilizing terrestrial SOPs for high-altitude aircraft navigation has been largely unstudied [51], [52], with most studies focusing on low-altitude UAVs [53], [54], [55], [56], [57]. To the authors' knowledge, the first comprehensive study assessing the potential of terrestrial cellular SOPs appeared in [58], [59], and [60]. The results therein were achieved from a collaboration between the United States Air Force (USAF) and the Autonomous Systems Perception, Intelligence, and Navigation (ASPIN) Laboratory through a week-long flight campaign called "SNIFFER: Signals of opportunity for Navigation In Frequency-Forbidden EnviRonments." ASPIN Laboratory's cellular SOP software-defined receivers (SDR) were flown on a Beechcraft C-12 Huron, a fixed-wing USAF aircraft, to collect ambient cellular signals for flight runs over three regions in California, USA: (i) Region A (rural): Edwards Air Force Base (AFB), (ii) Region B (semi-urban): Palmdale, and (iii) Region C: Riverside. The aircraft was equipped with an altimeter and an industrial-grade inertial measurement unit (IMU). The flights spanned different altitudes and a multitude of trajectories, including straight segments, banking turns, benign and aggressive maneuvers, and ascending/descending teardrops with a descent rate ranging between 0 to 1,500 ft/min. The flights were performed by members of the USAF Test Pilot School. The SDRs produced pseudorange measurements to cellular 3G code-division multiple-access (CDMA) and 4G long-term evolution (LTE) transmitters whose positions were mapped.

To showcase the viability of utilizing cellular SOP signals for aircraft navigation, the pseudoranges were fused via an extended Kalman filter (EKF), which utilized simple dynamical models to describe the aircraft's dynamics, namely a nearly constant velocity model and a Wiener process acceleration (WPA) model. Meter-level navigation accuracy was achieved on three flight runs [59], [60].

C. Summary of Contributions

This paper builds on the promising results presented in [59] and [60] by significantly extending these studies as follows:

- The assumption of known SOP transmitter position is relaxed, and a radio SLAM approach is adopted to evaluate the degradation in performance due to having to map the SOP positions simultaneously with navigating the aircraft. Different *a priori* conditions of the SOPs' positions are studied: from all unknown, to some known, to all known.
- Two radio SLAM frameworks are presented: (i) tightly-coupled SOP-aided INS and (ii) utilizing a WPA dynamical model for the aircraft's dynamics instead of the INS. The estimation performance was compared between

these two frameworks on the flight runs having IMU measurements.
- Intermittent pseudorange measurements along much longer (nearly double the length) trajectories are studied. This intermittent behavior of the measurements requires a re-initialization of the estimated clock error states in the radio SLAM framework.
- In contrast to previous radio SLAM studies in which GNSS signals were initially available [42], during which the EKF begins to map the SOP states before GNSS signals were cut off, this paper considers the more challenging scenarios of no GNSS conditions from the beginning. The only assumption is that the aircraft has an initial estimate of its own states.
- Theoretical and practical observations stemming from this unprecedented campaign are discussed along with considerations for the use of terrestrial SOPs in a radio SLAM fashion for high-altitude aircraft navigation.

Th paper presents results from four flight runs that took place over the rural (R), semi-urban (SU), and urban (U) regions, while exercising different aircraft maneuvers: holding (H), descending (D), and grid (G). In all cases, the SOPs' clock error states (bias and drift) were unknown and estimated alongside the aircraft's states. The results consistently demonstrated the promise of real-world aircraft navigation via radio SLAM, yielding bounded errors along trajectories of tens of kilometers. The three-dimensional (3-D) position root-mean squared errors (RMSEs) are summarized next, where N denotes the number of SOPs exploited along the trajectory: (1) SU, H, INS-SOP (WPA-SOP), $N = 6$, 56.7 km in 8.5 minutes, maximum altitude of 5,577 ft: 43.27 (47.39) m with all unknown and 10.14 (10.17) m with all known; (2) U, H, INS-SOP (WPA-SOP), $N = 6$, 72.7 km in 12.9 minutes, maximum altitude of 5,906 ft: 89.82 (79.44) m with all unknown and 16.97 (14.20) m with all known; (3) SU, D, WPA-SOP, $N = 18$, 111.9 km in 20.0 minutes, maximum altitude of 6,234 ft: 36.42 m with all unknown and 18.62 m with all known; and (4) R, G, WPA-SOP, $N = 32$, 78.4 km in 13.8 minutes, maximum altitude of 7,546 ft: 67.01 m with all unknown and 25.65 m with all known.

The rest of the paper is organized as follows. Section II describes the aircraft's kinematics and IMU measurement model, clock error dynamics, and pseudorange measurement model. Section III discusses the radio SLAM framework. Section IV overviews the aircraft hardware and software setup as well as the flight regions and aircraft maneuvers. Section V presents the experimental results of the four flight runs. Section VI gives concluding remarks.

II. Model Description

This sections presents the aircraft's kinematics and IMU measurements model, clock error states dynamics, and pseudorange measurement model.

A. Aircraft Kinematics

The aircraft's orientation, position, and velocity evolve in time according to the standard strapdown INS kinematic equations, driven by ${}^{b}\boldsymbol{\omega}_b$, a 3–D rotation rate vector of the body frame $\{b\}$ expressed in $\{b\}$, and ${}^{g}\boldsymbol{a}_b$, a 3–D acceleration vector of the body expressed in a global frame $\{g\}$ [61]. The 3–D orientation vector of $\{b\}$ with respect to $\{g\}$, denoted $\boldsymbol{\theta}_b$, and 3–D position $\boldsymbol{r}_b$ expressed in $\{g\}$ are related to ${}^{b}\boldsymbol{\omega}_b$ and ${}^{g}\boldsymbol{a}_b$ through the kinematic differential equations [61], [62]

$$\dot{\boldsymbol{\theta}}_b(t) = {}^{b}\boldsymbol{\omega}_b(t) \tag{1}$$

$$\ddot{\boldsymbol{r}}_b(t) = {}^{g}\boldsymbol{a}_b(t). \tag{2}$$

The aircraft-mounted IMU contains a triad-gyroscope and triad-accelerometer and produces angular rate $\boldsymbol{\omega}_{\text{imu}}$ and specific force $\boldsymbol{a}_{\text{imu}}$ measurements, which are modeled as [62]

$$\boldsymbol{\omega}_{\text{imu}}(k) = {}^{b}\boldsymbol{\omega}_b(k) + \boldsymbol{b}_{\text{g}}(k) + \boldsymbol{n}_{\text{g}}(k), \quad k = 1, 2, \ldots, \tag{3}$$

$$\boldsymbol{a}_{\text{imu}}(k) = \mathbf{R}_g^b(k)\left[{}^{g}\boldsymbol{a}_b(k) - {}^{g}\boldsymbol{g}(k)\right] + \boldsymbol{b}_{\text{a}}(k) + \boldsymbol{n}_{\text{a}}(k), \tag{4}$$

where $\mathbf{R}_g^b(k)$ is the rotation matrix from $\{g\}$ to $\{b\}$; ${}^{g}\boldsymbol{g}$ is the acceleration due to gravity in $\{g\}$; $\boldsymbol{b}_{\text{g}}$ and $\boldsymbol{b}_{\text{a}}$ are the gyroscope and accelerometer biases, respectively; and $\boldsymbol{n}_{\text{g}}$ and $\boldsymbol{n}_{\text{a}}$ are measurement noise vectors, which are modeled as white noise sequences with covariances $\mathbf{Q}_{\text{ng}}$ and $\mathbf{Q}_{\text{na}}$, respectively.

The gyroscope and accelerometer biases are assumed to evolve according to velocity random walk dynamics, namely

$$\boldsymbol{b}_{\text{g}}(k+1) = \boldsymbol{b}_{\text{g}}(k) + \boldsymbol{w}_{\text{bg}}(k) \tag{5}$$

$$\boldsymbol{b}_{\text{a}}(k+1) = \boldsymbol{b}_{\text{a}}(k) + \boldsymbol{w}_{\text{ba}}(k), \tag{6}$$

where $\boldsymbol{w}_{\text{bg}}$ and $\boldsymbol{w}_{\text{ba}}$ are bias instability process noise vectors, which are modeled as a discrete-time white noise sequences with covariances $\mathbf{Q}_{\text{bg}}$ and $\mathbf{Q}_{\text{ba}}$, respectively.

B. Aircraft Dynamics Model

If IMU measurements are not available or untrustworthy (e.g. due to a faulty gyroscope or accelerometer), a dynamics model can be used to model the aircraft's motion. The simple yet effective continuous Wiener process acceleration (WPA) model is chosen as its versatility allows for reliable propagation of the aircraft's states in different flight regimes (straight segments, coordinated maneuvers, etc.) [63]. Upon discretization at a constant sampling interval T, the aircraft's dynamics model is given by

$$\boldsymbol{x}_{\text{pva}}(k+1) = \mathbf{F}_{\text{pva}}\,\boldsymbol{x}_r(k) + \boldsymbol{w}_{\text{pva}}(k), \quad k = 0, 1, 2, \ldots, \tag{7}$$

$$\mathbf{F}_{\text{pva}} = \begin{bmatrix} \mathbf{I}_{3\times3} & T\mathbf{I}_{3\times3} & \frac{T^2}{2}\mathbf{I}_{3\times3} \\ \mathbf{0}_{3\times3} & \mathbf{I}_{3\times3} & T\mathbf{I}_{3\times3} \\ \mathbf{0}_{3\times3} & \mathbf{0}_{3\times3} & \mathbf{I}_{3\times3} \end{bmatrix},$$

where $\boldsymbol{x}_{\text{pva}} \triangleq \left[\boldsymbol{r}_r^{\mathsf{T}}, \dot{\boldsymbol{r}}_r^{\mathsf{T}}, \ddot{\boldsymbol{r}}_r^{\mathsf{T}}\right]^{\mathsf{T}}$, $\boldsymbol{r}_r \triangleq \left[x_r, y_r, z_r\right]^{\mathsf{T}}$ is the 3–D position of the aircraft expressed in a North-East-Down (NED) frame, and $\boldsymbol{w}_{\text{pva}}$ is a discrete-time zero-mean white noise sequence with covariance $\mathbf{Q}_{\text{pva}}$ given by

$$\mathbf{Q}_{\text{pva}} = \begin{bmatrix} \frac{T^5}{20} & \frac{T^4}{8} & \frac{T^3}{6} \\ \frac{T^4}{8} & \frac{T^3}{3} & \frac{T^2}{2} \\ \frac{T^3}{6} & \frac{T^2}{2} & T \end{bmatrix} \otimes \tilde{\mathbf{S}}_{\text{NED}},$$

where $\otimes$ denotes the Kronecker product, and $\tilde{\mathbf{S}}_{\text{NED}} \triangleq \text{diag}\left[\tilde{q}_N, \tilde{q}_E, \tilde{q}_D\right]$, where $\tilde{q}_N, \tilde{q}_E$, and $\tilde{q}_D$ are the NED jerk continuous-time noise power spectra, respectively. Of course, alternative more complicated dynamic models can be adopted to describe the aircraft's dynamics (e.g., Singer acceleration, mean-adaptive acceleration, circular motion, curvilinear motion, coordinated turn, among others [63]).

C. SOP Dynamics Model

The SOPs considered herein are stationary, therefore

$$\boldsymbol{r}_{\text{sop}_l}(k+1) = \boldsymbol{r}_{\text{sop}_l}(k), \quad l = 1, \ldots, L, \tag{8}$$

where $\boldsymbol{r}_{\text{sop}_l}$ is the l-th SOP's 3–D position vector and L is the total number of SOPs used to perform radio SLAM.

D. Clock Dynamics Model

The receiver's and SOPs' clock error state dynamics are assumed evolve according to the standard double integrator, driven by process noise, namely [64].

$$\boldsymbol{x}_{\text{clk},i}(k+1) = \mathbf{F}_{\text{clk}}\, \boldsymbol{x}_{\text{clk},i}(k) + \boldsymbol{w}_{\text{clk},i}(k), \tag{9}$$

$$\boldsymbol{x}_{\text{clk},i} \triangleq \left[\, c\delta t_i,\, c\dot{\delta} t_i \,\right]^{\mathsf{T}}, \quad \mathbf{F}_{\text{clk}} = \begin{bmatrix} 1 & T \\ 0 & 1 \end{bmatrix},$$

where $i = \{\text{r}, \text{sop}\}$, δt_i is the clock bias, $\dot{\delta} t_i$ is the clock drift, c is the speed of light, T is the constant sampling interval, and $\boldsymbol{w}_{\text{clk},i}$ is the process noise, which is modeled as a discrete-time white noise sequence with covariance

$$\mathbf{Q}_{\text{clk},i} = c^2 \cdot \begin{bmatrix} S_{\tilde{w}_{\delta t_i}} T + S_{\tilde{w}_{\dot{\delta} t_i}} \frac{T^3}{3} & S_{\tilde{w}_{\dot{\delta} t_i}} \frac{T^2}{2} \\ S_{\tilde{w}_{\dot{\delta} t_i}} \frac{T^2}{2} & S_{\tilde{w}_{\dot{\delta} t_i}} T \end{bmatrix}, \tag{10}$$

The terms $S_{\tilde{w}_{\delta t_i}}$ and $S_{\tilde{w}_{\dot{\delta} t_i}}$ are the clock bias and drift process noise power spectral densities (PSDs), respectively, which can be related to the power-law coefficients, $\{h_{\alpha_i}\}_{\alpha_i=-2}^{2}$, which have been shown through laboratory experiments to characterize the power spectral density of the fractional frequency deviation of an oscillator from nominal frequency according to $S_{\tilde{w}_{\delta t_i}} \approx \frac{h_{0,i}}{2}$ and $S_{\tilde{w}_{\dot{\delta} t_i}} \approx 2\pi^2 h_{-2,i}$ [65]. The receiver's and SOPs' process noise covariances $\mathbf{Q}_{\text{clk}_\text{r}}$ and $\mathbf{Q}_{\text{clk}_\text{sop}}$ are calculated from (10) using the PSDs associated with the receiver's and SOPs' oscillator quality, respectively.

The dynamics of the difference between the receiver's and SOPs' clock error states is given by

$$\begin{aligned} \boldsymbol{\Delta x}_{\text{clk}}(k+1) =& \mathbf{F}_{\boldsymbol{\Delta}\text{clk}} \boldsymbol{\Delta x}_{\text{clk}}(k) + \boldsymbol{\Delta w}_{\text{clk}}(k), \\ \boldsymbol{\Delta x}_{\text{clk}} \triangleq& \left[c\Delta\delta t_{\text{sop}_1}, c\Delta\dot{\delta} t_{\text{sop}_1}, \ldots, c\Delta\delta t_{\text{sop}_L}, c\Delta\dot{\delta} t_{\text{sop}_L}\right]^{\mathsf{T}}, \\ c\Delta\delta t_{\text{sop}_l} \triangleq& c \cdot \left[\delta t_\text{r} - \delta t_{\text{sop}_l}\right], \quad c\Delta\dot{\delta} t_{\text{sop}_l} \triangleq c \cdot \left[\dot{\delta} t_\text{r} - \dot{\delta} t_{\text{sop}_l}\right], \end{aligned} \tag{11}$$

$\mathbf{F}_{\boldsymbol{\Delta}\text{clk}} = \mathbf{I}_{L\times L} \otimes \mathbf{F}_{\text{clk}}$, with $\otimes$ denoting the Kronecker product, and $\boldsymbol{\Delta w}_{\text{clk}}$ is the process noise which has a covariance $\mathbf{Q}_{\boldsymbol{\Delta}\text{clk}}$ that encapsulates the correlation between entries of $\boldsymbol{\Delta x}_{\text{clk}}$ resulting from the common process noise of the receiver clock states. Assuming the SOP towers to be equipped with oscillators of identical quality, $\mathbf{Q}_{\boldsymbol{\Delta}\text{clk}}$ simplifies to

$$\mathbf{Q}_{\boldsymbol{\Delta}\text{clk}} = \mathbb{1}_{L\times L} \otimes \mathbf{Q}_{\text{clk}_\text{r}} + \mathbf{I}_{L\times L} \otimes \mathbf{Q}_{\text{clk}_\text{sop}},$$

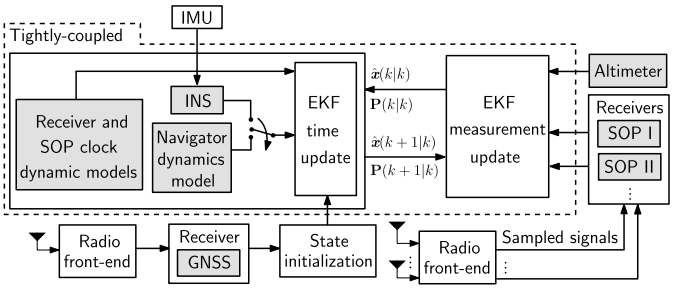

Fig. 1. Overview of a tightly-coupled radio SLAM framework. The radio front-end collects signals, which are processed in the navigation receivers. The EKF is initialized with GNSS receiver estimates. The EKF time update is performed based on the toggling switch: (i) using a dynamical model that describes the navigator's dynamics or (ii) using an INS, when available. The EKF measurement update is performed using navigation observables from received SOP signals and altimeter measurements.

where $\mathbb{1}_{L\times L}$ is the $L \times L$ matrix with all entries equal to 1 and $\mathbf{I}_{L\times L}$ is the $L \times L$ identity matrix.

E. Pseudorange Measurement Model

The aircraft-mounted SOP receiver extracts pseudorange measurements ρ from the received signals by estimating the time-of-arrival. The pseudorange ρ_l from the l-th SOP transmitter at time-step k is modeled as [43]

$$\begin{aligned} \rho_l(k) =& \left\| \boldsymbol{r}_\text{r}(k) - \boldsymbol{r}_{\text{sop}_l}(k) \right\|_2 \\ &+ c \cdot \left[\delta t_\text{r}(k) - \delta t_{\text{sop}_l}(k)\right] + v_{\rho_l}(k), \end{aligned} \tag{12}$$

where $\boldsymbol{r}_\text{r}$ and $\boldsymbol{r}_{\text{sop}_l}$ are the receiver's and l-th SOP's 3–D position vectors expressed in the same reference frame, respectively; δt_r and δt_{sop_l} are the receiver's and l-th SOP transmitter's clock biases, respectively; and v_{ρ_l} is the pseudorange measurement noise, which is modeled as a white Gaussian random sequence with variance $\sigma^2_{\rho_l}(k)$. The reader is referred to [59], which assessed the pseudoranges from terrestrial cellular SOPs, showing that they are nearly multipath-free when received by high-altitude aircraft.

III. Radio SLAM Framework

The radio SLAM framework aims at exploiting ambient SOPs whenever GNSS signals become unavailable or untrustworthy. Even though the SOP transmitter locations may not be known precisely, radio SLAM allows for GNSS-less navigation by simultaneously estimating the SOPs' position and clock error states in addition to the vehicle's states. The block diagram of the radio SLAM framework is shown in Fig. 1. The remainder of this section formulates the radio SLAM framework that fuses pseudorange measurements $\boldsymbol{z} \triangleq [\rho_1, \ldots, \rho_L]^{\mathsf{T}}$ extracted from SOPs in a tightly-coupled fashion with INS (if IMU measurements are available) or with an assumed navigator dynamical model. The two radio SLAM frameworks, with INS or with WPA dynamical model, are identical except for the mechanization used in the EKF propagation step. It is worth emphasizing that while an EKF is chosen in this paper, other nonlinear filters can be adopted in the block diagram of Fig. 1.

A. EKF State Vector

If IMU rotation rate and specific force measurements are available, the EKF state vector propagated via INS equations is given by

$$\boldsymbol{x}_{\text{ins}} = \left[\boldsymbol{x}_{\text{r,ins}}^{\mathsf{T}},\, \boldsymbol{x}_{\text{sop}_1}^{\mathsf{T}},\, \ldots,\, \boldsymbol{x}_{\text{sop}_L}^{\mathsf{T}}\right]^{\mathsf{T}}$$
$$\boldsymbol{x}_{\text{r,ins}} = \left[{}^{b}_{g}\bar{\boldsymbol{q}}^{\mathsf{T}},\, \boldsymbol{r}_{\text{r}}^{\mathsf{T}},\, \dot{\boldsymbol{r}}_{\text{r}}^{\mathsf{T}},\, \boldsymbol{b}_{\text{g}}^{\mathsf{T}},\, \boldsymbol{b}_{\text{a}}^{\mathsf{T}}\right]^{\mathsf{T}}$$
$$\boldsymbol{x}_{\text{sop}_l} = \left[\boldsymbol{r}_{\text{sop}_l}^{\mathsf{T}},\, c\Delta\delta t_{\text{sop}_l},\, c\Delta\dot{\delta} t_{\text{sop}_l}\right]^{\mathsf{T}},$$

where $\boldsymbol{x}_{\text{r,ins}}$ is the vehicle's state vector, composed of ${}^{b}_{g}\bar{\boldsymbol{q}} \triangleq \left[{}^{b}_{g}\boldsymbol{q}^{\mathsf{T}},\, {}^{b}_{g}q\right]^{\mathsf{T}}$, which is a 4–D unit quaternion representing the orientation of $\{b\}$ fixed at the IMU with respect to $\{g\}$, $\boldsymbol{r}_{\text{r}}$ and $\dot{\boldsymbol{r}}_{\text{r}}$ are the 3–D position and velocity of the vehicle expressed in $\{g\}$, and $\boldsymbol{b}_{\text{g}}$ and $\boldsymbol{b}_{\text{a}}$ are 3–D biases of the IMU's gyroscopes and accelerometers, respectively, expressed in $\{b\}$. Quaternions were chosen to represent the orientation of the vehicle with respect to $\{g\}$, since they offer minimal attitude representation without suffering from the singularity of other mathematical attitude representations (e.g., Euler angles). However, since the 4–D quaternion is an overdetermined representation of attitude, the estimation error covariance associated with orientation is represented by a 3×3 matrix corresponding to a three-axis error angle vector to prevent degeneracy. The vector $\boldsymbol{x}_{\text{sop}_l}$ is the l-th SOP transmitter state vector, composed of the SOP tower's 3–D position $\boldsymbol{r}_{\text{sop}_l}$ vector expressed in $\{g\}$, and the difference between the receiver's and l-th SOP transmitter's clock bias $c\Delta\delta t_{\text{sop}_l}$ and drift $c\Delta\dot{\delta} t_{\text{sop}_l}$.

When IMU measurements are unavailable or untrustworthy, the WPA dynamics model is adopted, leading to the EKF state

$$\boldsymbol{x}_{\text{pva}} = \left[\boldsymbol{x}_{\text{r,pva}}^{\mathsf{T}},\, \boldsymbol{x}_{\text{sop}_1}^{\mathsf{T}},\, \ldots,\, \boldsymbol{x}_{\text{sop}_L}^{\mathsf{T}}\right]^{\mathsf{T}}$$
$$\boldsymbol{x}_{\text{r,pva}} = \left[\boldsymbol{r}_{\text{r}}^{\mathsf{T}},\, \dot{\boldsymbol{r}}_{\text{r}}^{\mathsf{T}},\, \ddot{\boldsymbol{r}}_{\text{r}}^{\mathsf{T}}\right]^{\mathsf{T}}.$$

B. EKF Time Update

The EKF time update step produces an estimate $\hat{\boldsymbol{x}}(k|j) \triangleq \mathbb{E}[\boldsymbol{x}(k)|\boldsymbol{Z}^j]$ of $\boldsymbol{x}(k)$, and an associated estimation error covariance $\mathbf{P}_{\boldsymbol{x}}(k|j)$, where $\mathbb{E}[\cdot|\cdot]$ denotes the conditional expectation, $\boldsymbol{Z}^j \triangleq \{\boldsymbol{z}(i)\}_{i=1}^{j}$ is the set of measurements available up to and including time index j, and $k > j$.

For INS propagation, the IMU measurements (3) and (4) are processed through a vector-valued function of strapdown INS equations in $\{g\}$ that discretize (1) and (2) to obtain

$$\hat{\boldsymbol{x}}_{\text{r,ins}}(k+1|j) = \boldsymbol{f}_{\text{ins}}^{\{g\}}\left[\hat{\boldsymbol{x}}_{\text{r,ins}}(k|j), \boldsymbol{\omega}_{\text{imu}}(k), \boldsymbol{a}_{\text{imu}}(k)\right],$$

where the gyroscope and accelerometer bias time update $\hat{\boldsymbol{b}}_{\text{g}}(k+1|j)$ and $\hat{\boldsymbol{b}}_{\text{a}}(k+1|j)$ follow from (5) and (6), respectively [42], [62]. The INS mechanization equations are performed with the Earth-centered Earth-fixed (ECEF) frame (denoted $\{e\}$) as $\{g\}$, since any information about the SOP transmitters' positions would be available in the ECEF global frame. The ECEF INS strapdown mechanization equations are given in Appendix A and their linearization to propagate the estimation error covariance are detailed in Appendix B. The time update of the differenced clock states between the receiver and the SOP transmitters follow from (11).

If INS data is not available, the WPA dynamics model in (7) is used for EKF time update to yield $\hat{\boldsymbol{x}}_{\text{r,pva}}(k+1|j)$.

The EKF time update of the SOP states $\left\{\boldsymbol{x}_{\text{sop}_l}\right\}_{l=1}^{L}$ can be readily computed from (8) and (11).

C. EKF Update

The aircraft-mounted receiver makes pseudorange measurements $\boldsymbol{z}$, modeled as (12), which are ingested in the EKF update step to correct the prior state estimate $\hat{\boldsymbol{x}}(k|j)$, producing an updated estimate $\hat{\boldsymbol{x}}(k|k)$ and an associated posterior estimation error covariance $\mathbf{P}_{\boldsymbol{x}}(k|k)$. Details on the INS EKF update equations to remedy the discrepancy between the 4–D estimated quaternion and the associated 3×3 covariance matrix are given in Appendix C. The standard EKF update equations are implemented when propagating the states using the WPA dynamics model (7).

IV. SNIFFER: Hardware Setup and Flight Regions

This section overviews the hardware setup used for data collection and processing in the SNIFFER flight campaign. It also describes the flight regions and aircraft maneuvers.

A. Hardware and Software Setup

The hardware was assembled on a rack, which was mounted on the C-12 aircraft. The rack was equipped with

- A quad-channel universal software radio peripheral (USRP)-2955.
- A desktop computer equipped with solid-state drive for data storage.
- A laptop computer running real-time cellular SOP acquisition, which was operated during the flight by a flight engineer to determine when, where, and what cellular LTE channels were available to tune the USRP-2955 accordingly. The USRP-2955 was connected to the laptop via a peripheral component interconnect express (PCIe) cable.
- A GPS antenna to (i) feed GPS measurements to the aircraft navigation system and (ii) discipline the USRP's on-board GPS-disciplined oscillator (GPSDO).

Three consumer-grade 800/1900 MHz Laird cellular antennas were mounted to the bottom of the C-12 and were connected to the USRP-2955. The USPR was tuned to listen to carrier frequencies corresponding to the U.S. cellular providers: T-Mobile, AT&T, and Verizon. The sampling rate of each cellular channel was 10 mega samples per second (Msps). The receivers described in [66] and [67] were used to produce pseudorange measurements to cellular 3G CDMA and 4G LTE SOPs, respectively. Fig. 2 shows the C-12 aircraft, known as Ms. Mabel, along with ASPIN researchers and USAF pilots. Fig. 3 shows the hardware setup with which the C-12 aircraft was equipped.

The C-12 flew at various altitudes and performed three types of maneuvers, illustrated in Fig. 5: holding pattern, climbing/descending teardrop-like pattern, and grid-like pattern.

Fig. 2. USAF Pilots and ASPIN researchers with the C-12 aircraft. Left to right: Hulsey, Tay, Abdallah, Quirarte, Kassas, Khalife, Hoeffner, and Wachtel.

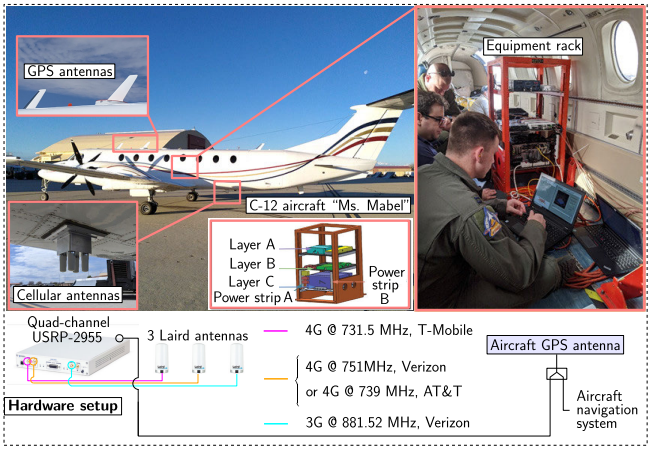

Fig. 3. Hardware setup with which the C-12 aircraft was equipped.

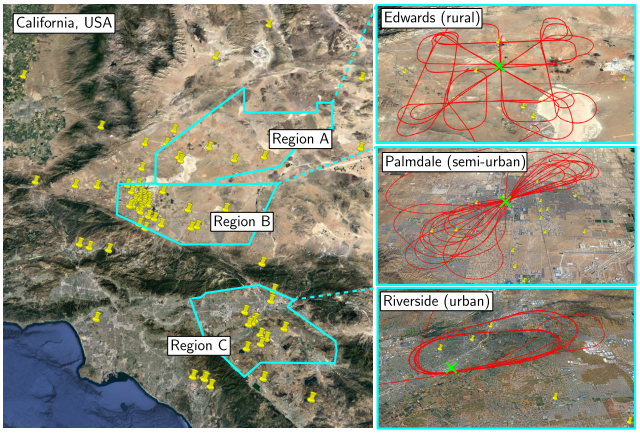

Fig. 4. The three regions over which the flight campaign took place. The yellow pins represent cellular towers. The flight trajectories are shown in red.

B. Flight Regions and Aircraft Maneuvers

A flight campaign over four consecutive days was conducted during which samples of cellular SOPs were stored for post-processing. The flights took place over three regions in California, USA, shown in Fig. 4: (i) Region A (rural): Edwards AFB, (ii) Region B (semi-urban): Palmdale, and (iii) Region C (urban): Riverside.

V. Experimental Results

This section presents extensive experimental radio SLAM results for the 4 different flight runs summarized in Table I. In the first 2 runs, IMU measurements were available. As such,

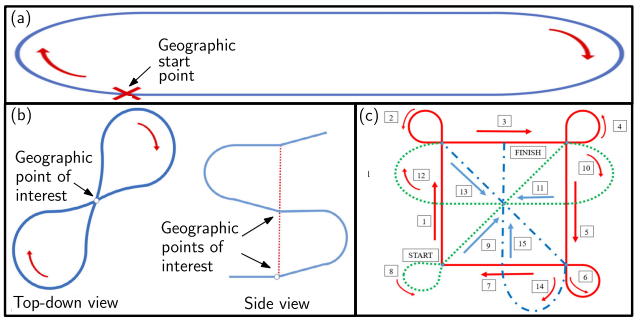

Fig. 5. Maneuvers performed by the C-12 aircraft: (a) holding, (b) teardrop ascending/descending, and (c) grid.

TABLE I
Experimental Flight Runs

	Run 1	Run 2	Run 3	Run 4
Region	Semi-urban	Urban	Semi-urban	Rural
Maneuver	Holding Pattern	Holding Pattern	Descending Teardrop	Grid Pattern
Kinematics	INS	INS	WPA	WPA
Number of SOPs	6	6	18	32
Cellular SOPs	3G	3G	4G	4G
Cellular frequencies (MHz)	881.52	881.52	731.5 739	731.5 739 751
Duration (min)	8.5	12.9	20.0	13.8
Distance (km)	56.7	72.7	111.9	78.4
Altitude (ft)	5,577	5,906	3,709 – 6,234	6,234 – 7,546
Avg. speed (km/h)	401.7	337.4	335.5	340.1

the SOP-INS radio SLAM framework was implemented to navigate the aircraft. Pseudorange measurements from cellular 3G SOPs were used in these runs, which were continuously available throughout the flight trajectory. In the last 2 runs, IMU measurements were not available. Consequently, the WPA model was adopted in the radio SLAM framework. Pseudorange measurements from cellular 4G LTE SOPs were used in these runs, which were intermittently available along the flight trajectory. It is worth noting that Table I lists the number of SOPs used by the radio SLAM filter in each flight run. It is not representative of the total number of SOPs available in each region. Additionally, a different implementation of the opportunistic receiver that extracts the pseudorange measurements was used to process 3G and 4G signals. The different settings in each receiver implementation explains the fact that there are more 4G SOPs than 3G ones, but at the expense of measurement continuity.

It is worth mentioning that in this experimental proof of concept, the radio SLAM navigation algorithms were applied in a post-processing fashion. The pseudorange measurements, time-stamped by the receiver opportunistically extracting them, were aligned and used in conjunction with the time-stamped specific force and angular rate measurements produced by the IMU in the radio SLAM filter. The resulting

radio SLAM navigation solution was compared to the time-stamped ground truth solution provided by the US Air Force's on-board Honeywell H764-ACE EGI INS/GPS. The next subsection summarizes the navigation filter initialization and settings. Next experimental results for each flight run are presented along with accompanying analysis and discussion.

A. Filter Initialization and Settings

The aircraft's orientation, position, velocity, and acceleration state estimates were initialized in ECEF by corrupting the aerial vehicle's true initial states (obtained from the aircraft's on-board Honeywell H764-ACE EGI INS/GPS system) with a random sample $\tilde{\boldsymbol{x}}_{\mathrm{r}}(0|0)$ drawn from a zero-mean multivariate Gaussian distribution with covariance $\mathbf{P}_{\boldsymbol{x}_{\mathrm{r}}}(0|0)$. For radio SLAM with an INS, the orientation, position, and velocity states were initialized as

$$\begin{aligned}\tilde{\boldsymbol{x}}_{\boldsymbol{qr\dot{r}},\mathrm{ins}}(0|0) &\sim \mathcal{N}\left[\mathbf{0}_{9\times 1},\ \mathbf{P}_{\boldsymbol{qr\dot{r}},\mathrm{ins}}(0|0)\right]\\ \mathbf{P}_{\boldsymbol{qr\dot{r}},\mathrm{ins}}(0|0) &= \left[(10^{-2})\cdot\mathbf{I}_{3\times 3},\,(10)\cdot\mathbf{I}_{3\times 3},\,\mathbf{I}_{3\times 3}\right],\end{aligned} \tag{13}$$

where $\mathbf{P}_{\boldsymbol{qr\dot{r}},\mathrm{ins}}(0|0)$ is the initial covariance of the aircraft's orientation, position, and velocity with units of [rad^2, m^2, (m/s)^2]. The IMU gyroscope and accelerometer biases; $\boldsymbol{b}_{\mathrm{g}}$ and $\boldsymbol{b}_{\mathrm{a}}$, respectively; were initialized to $\boldsymbol{b}_{\mathrm{g}} = \boldsymbol{b}_{\mathrm{a}} = \mathbf{0}$ with covariance $\mathbf{P}_{\boldsymbol{b}_{\mathrm{imu}}}(0|0) = \left[(10^{-3})\cdot\mathbf{I}_{3\times 3},\,(10^{-2})\cdot\mathbf{I}_{3\times 3}\right]$ with units of [(rad/s)^2, (m/s^2)^2].

The first three components of $\tilde{\boldsymbol{x}}_{\boldsymbol{qr\dot{r}},\mathrm{ins}}(0|0)$, which correspond to the vector of angle errors, were used to corrupt the true initial Euler angles of the aircraft. The corrupted initial Euler angles were then converted to a unit quaternion to initialize the EKF's orientation states. The remaining position and velocity elements of the initial aircraft's state estimates were corrupted by adding the corresponding initial error terms to the true initial states.

For radio SLAM with the WPA dynamics model, the initialization scheme for the aircraft's position, velocity, and acceleration states is given by

$$\begin{aligned}\tilde{\boldsymbol{x}}_{\boldsymbol{r\dot{r}\ddot{r}},\mathrm{pva}}(0|0) &\sim \mathcal{N}\left[\mathbf{0}_{9\times 1},\ \mathbf{P}_{\boldsymbol{r\dot{r}\ddot{r}},\mathrm{pva}}(0|0)\right]\\ \mathbf{P}_{\boldsymbol{r\dot{r}\ddot{r}},\mathrm{pva}}(0|0) &= \left[(10)\cdot\mathbf{I}_{3\times 3},\,\mathbf{I}_{3\times 3},\,(10^{-2})\cdot\mathbf{I}_{3\times 3}\right],\end{aligned} \tag{14}$$

where $\mathbf{P}_{\boldsymbol{r\dot{r}\ddot{r}},\mathrm{pva}}(0|0)$ is the initial aerial vehicle position, velocity, and acceleration covariance with units of [m^2, (m/s)^2, (m/s^2)^2].

The l-th cellular SOP's position state estimate $\hat{\boldsymbol{r}}_{\mathrm{sop},l}(0|0)$ was initialized in the ECEF frame as

$$\begin{aligned}\hat{\boldsymbol{r}}_{\mathrm{sop},l}(0|0) &\sim \mathcal{N}\left[\boldsymbol{r}_{\mathrm{sop},l},\ \mathbf{P}_{\boldsymbol{r}_{\mathrm{sop}}}(0|0)\right]\\ \mathbf{P}_{\boldsymbol{r}_{\mathrm{sop}}}(0|0) &= \mathbf{R}_n^e\,\mathbf{P}^n_{\boldsymbol{r}_{\mathrm{sop}}}(0|0)\,\left[\mathbf{R}_n^e\right]^{\mathsf{T}},\end{aligned}$$

where $\boldsymbol{r}_{\mathrm{sop},l}$ is the l-th cellular SOP tower's true position in ECEF and $\mathbf{P}_{\boldsymbol{r}_{\mathrm{sop}}}(0|0)$ is the associated initial covariance; $\mathbf{P}^n_{\boldsymbol{r}_{\mathrm{sop}}}(0|0)$ is the initial cellular SOP tower's position covariance in a local North-East-Down (NED) frame denoted $\{n\}$; and $\mathbf{R}_n^e$ is the fixed rotation matrix from local NED frame to the global ECEF frame.

The filter clock error states $\boldsymbol{\Delta x}_{\mathrm{clk}}$ consisted of the difference between the receiver and each cellular SOP's clock error states.

TABLE II
AIRCRAFT'S INDUSTRIAL-GRADE IMU NOISE PARAMETERS

	Gyroscope	Accelerometer
Bias Instability	$2^\circ/\mathrm{hr}$	$1\,mg$
Noise Density	$15^\circ/\mathrm{hr}/\sqrt{\mathrm{Hz}}$	$3.2\,\mathrm{mg}/\sqrt{\mathrm{Hz}}$

TABLE III
OSCILLATOR PARAMETERS

Quality	Coefficients $\{h_0,\ h_{-2}\}$
Typical-quality TCXO	$\{9.4\times10^{-20},\ 3.8\times10^{-21}\}$
Typical-quality OCXO	$\{8.0\times10^{-20},\ 4.0\times10^{-23}\}$

The filter's clock bias state estimates were initialized by subtracting the estimated range from the measured pseudorange while the filter's clock drift state estimates were initialized to 0. The initial filter's clock states' covariance was set to $\mathbf{P}_{\boldsymbol{\Delta x}_{\mathrm{clk}}} = \mathbf{I}_{L\times L}\otimes\left[10^4,\ 1\right]$ with units of [m^2, (m/s)^2] for the differenced clock bias and drift, respectively.

The gyroscope and accelerometer bias instability process noise covariances are expressed as $\mathbf{Q}_{\mathrm{bg}} = \sigma^2_{\mathrm{bg}}\mathbf{I}_{3\times 3}$ and $\mathbf{Q}_{\mathrm{ba}} = \sigma^2_{\mathrm{ba}}\mathbf{I}_{3\times 3}$, where σ^2_{bg} and σ^2_{ba} are computed by squaring the bias instability parameters of Table II, expressed in rad/s and m/s^2, respectively. The gyroscope and accelerometer measurement noise covariances are expressed as $\mathbf{Q}_{\mathrm{ng}} = \sigma^2_{\mathrm{ng}}\mathbf{I}_{3\times 3}$ and $\mathbf{Q}_{\mathrm{na}} = \sigma^2_{\mathrm{na}}\mathbf{I}_{3\times 3}$, where σ^2_{ng} and σ^2_{na} are computed by first multiplying the noise density parameters of Table II by the square root of the IMU sampling rate and then squaring the resulting quantities expressed in rad/s and m/s^2, respectively. These noise parameters correspond to an industrial-grade IMU and are used to compute the INS process noise covariance matrix as detailed in Appendix B.

For the WPA dynamics model, the jerk process noise spectra were chosen to be $\tilde{q}_N = \tilde{q}_E = 10$ m^2/s^5 and $\tilde{q}_D = 1$ m^2/s^5 in the local NED frame. This process noise covariance was rotated to the global ECEF frame, in which the aircraft states are estimated, before being fed to the EKF time update step.

The clocks process noise covariances were set to correspond to a typical-quality temperature-compensated crystal oscillator (TCXO) for the receiver and a typical-quality oven-controlled crystal oscillator (OCXO) for the SOPs. The power-law coefficients of these oscillators are given in Table III.

Altimeter updates were performed throughout the flight by fusing the altimeter measurements from the aircraft's on-board navigation system into the radio SLAM EKF. The altimeter measurements noise variance was set to $\sigma^2_{\mathrm{alt}} = 3$ m^2.

The time-varying cellular SOP pseudoranges measurement noise variances $\sigma^2_{\rho_l}(k)$ were set to be inversely proportional to the C/N_0, expressed in linear units, as estimated by the receivers in [66] and [67]. The range of values taken by the measurement noise variances are stated for each run in the subsequent subsections.

The initial cellular SOP tower's position covariances in the local NED frame $\mathbf{P}^n_{\boldsymbol{r}_{\mathrm{sop}}}(0|0)$ was set to $\left[10^5, 10^5, 10^2\right]$ m^2 for flight runs 1 and 2 and to $\left[10^4, 10^4, 10^2\right]$ m^2 for flight runs 3 and 4, which correspond to an initial 2–D 95%

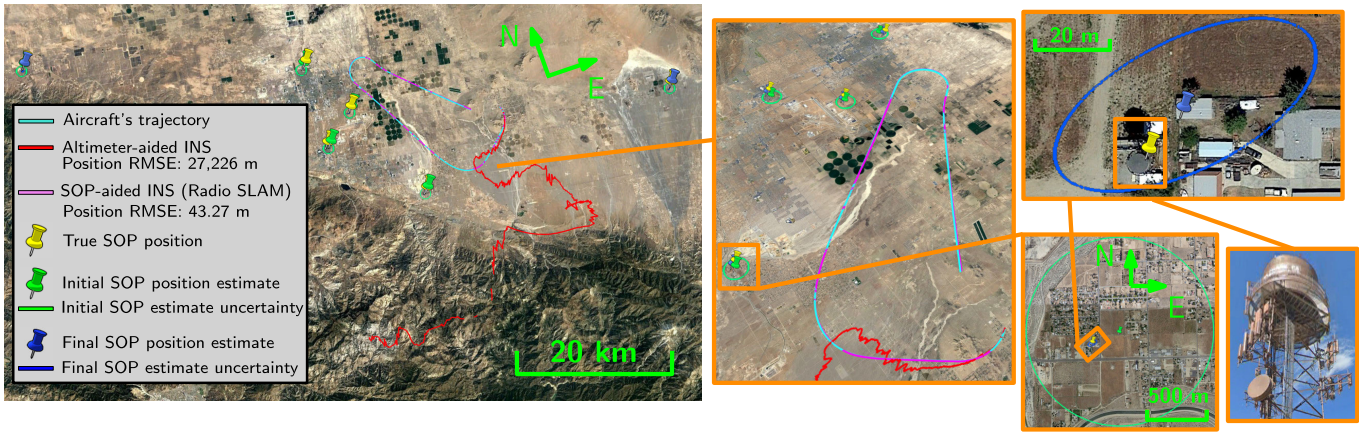

Fig. 6. Left: Flight Run 1 aircraft's true (cyan) and estimated trajectories: (i) SOP-INS radio SLAM with all 6 SOPs unknown (magenta) and (ii) altimeter-aided INS (red). Right: The initial SOP position estimate (green pin) has a 2–D error of 263.65 m (in the North-East plane) with respect to the true SOP position (yellow pin) while the final SOP position estimate (blue pin) converged to within 19.38 m from the actual tower after performing radio SLAM for SOP 2. Map data: Google Earth.

uncertainty circle of radius 774 and 245 m, respectively, in the North-East plane.

It is worth noting that each flight run was processed with radio SLAM EKFs having various levels of *a priori* knowledge of the cellular SOP towers' positions. To ensure a fair comparison between the different filters, all the uncertain states common to both filters (including aircraft and SOP states) were initialized with the same error. In the following, n will refer to the number of SOPs with known positions and m will refer to the number of SOPs with unknown positions, where $n+m=L$, with L being the total number of SOPs. Additionally, "known" SOPs means that the filter has knowledge of the tower position only, as there was no way of knowing the tower clock states, which had to be estimated in all cases.

B. Radio SLAM With INS

An EKF was implemented to perform radio SLAM, while aiding the aircraft's INS with pseudorange measurements extracted from ambient cellular SOPs. The IMU measurements were taken to be trustworthy in this proof of concept and were integrated at a rate of 100 Hz during propagations using the mechanization equations of Appendix A. A more mature implementation of this framework would have redundancy in the sensors (i.e., multiple IMUs on-board the aircraft) and advanced fault detection and exclusion algorithms to detect untrustworthy IMU measurements considering the safety-criticality of this application. If a defect is detected in the gyroscopes or accelerometers, the on-board logic can fall back to the WPA dynamical model. The fusion of the opportunistically extracted pseudoranges was performed at a rate of 5 Hz during the EKF's update step. The experimental navigation results for flight runs 1 and 2 are presented next.

1) Flight Run 1: The flight trajectory for Run 1 consisted of a holding pattern with the following segments: (i) a 70° banking turn over 5 km, (ii) an 8-km straight segment, (iii) a 90° banking turn over 7 km, (iv) a 21-km straight segment, (v) a 180° banking turn over 8 km, and (vi) an 18-km straight segment. The aircraft flew a 56.7-km trajectory in 8.5 minutes at an average altitude of 5,577 ft above ground level (AGL) and an average speed of 401.7 km/h over a semi-urban region as summarized in Table I. The receiver on-board the aircraft extracted pseudorange measurements from 6 cellular 3G SOPs for the entire duration of the flight run. The minimum and maximum distances from the aircraft to any SOP tower over the trajectory were 4.19 and 72.62 km, respectively, and the average distance from the aircraft to the SOP towers ranged from 12.73 to 60.42 km for the closest and furthest towers, respectively. The 3G pseudorange measurement noise variances σ_ρ^2 for flight Run 1 varied between 0.0004 m^2 and 0.66 m^2.

TABLE IV
FLIGHT RUN 1 EXPERIMENTAL RESULTS

	Altimeter-INS	**Radio SLAM** ($n=0$, $m=6$)	**Radio SLAM** ($n=2$, $m=4$)	**Radio SLAM** ($n=6$, $m=0$)
Attitude RMSE (°)	143.68	3.01	3.30	3.32
Final Att. Error (°)	128.96	2.80	1.88	2.20
Max. Att. Error (°)	299.97	13.20	13.26	13.27
Position RMSE (m)	27,226	43.27 (47.39)	28.20 (26.20)	10.14 (10.17)
Final Pos. Error (m)	37,011	78.77 (80.61)	43.67 (34.47)	2.81 (7.13)
Max. Pos. Error (m)	41,425	79.29 (82.50)	45.25 (52.77)	39.64 (36.79)
Velocity RMSE (m/s)	203.17	0.67 (0.94)	0.53 (0.83)	0.47 (0.80)
Final Vel. Error (m/s)	242.91	0.86 (0.88)	0.68 (0.64)	0.51 (0.51)
Max. Vel. Error (m/s)	271.64	2.20 (3.07)	1.82 (2.99)	1.99 (2.99)

Table IV summarizes flight Run 1's navigation performance of the altimeter-INS filter, the SOP-INS, and WPA (in parentheses) radio SLAM frameworks with varying levels of *a priori* knowledge on the SOP towers' true positions.

Fig. 6 shows the aircraft's true trajectory, altimeter-INS trajectory, and SOP-INS radio SLAM (with $n=0$ known towers and $m=6$ unknown towers) trajectory for flight Run 1.

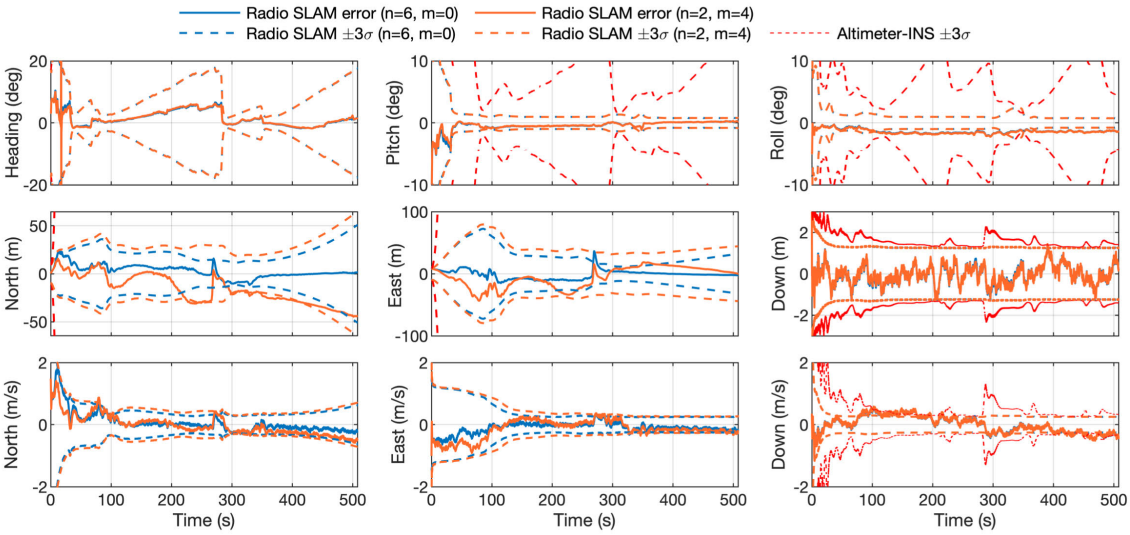

Fig. 7. EKF plots of the time history of the aircraft's states estimation errors and associated $\pm 3\sigma$ bounds for a filter implementing the INS radio SLAM framework on flight Run 1 with $n = 6$ known towers and $m = 0$ unknown towers (blue) and $n = 2$ known towers and $m = 4$ unknown towers (orange) as well as the $\pm 3\sigma$ bounds for an altimeter-INS filter (red). The first row corresponds to the orientation states of the aircraft's body frame with respect to the NED frame represented using Euler angles. The second and third rows correspond to the aircraft's position and velocity states in the NED frame, respectively.

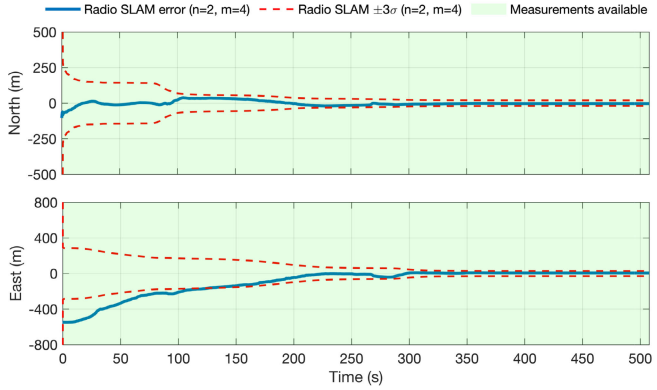

Fig. 8. Flight Run 1 EKF plots of the time history of the horizontal position estimation errors in the North-East plane and associated $\pm 3\sigma$ bounds for SOP 1 for the INS radio SLAM filter with $n = 2$ known towers and $m = 4$ unknown towers. Pseudoranges were extracted from SOP 1's 3G signals by the on-board receiver for the entirety of flight Run 1.

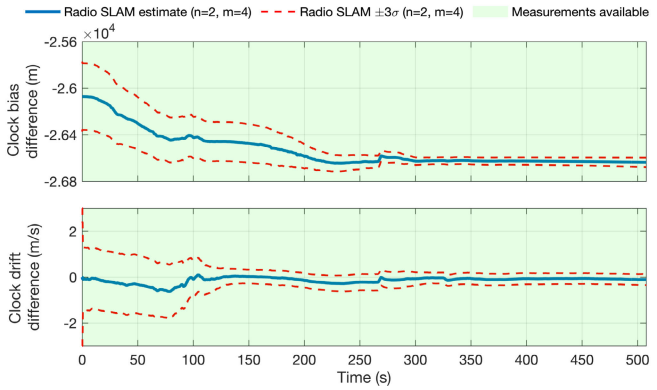

Fig. 9. Flight Run 1 EKF plots of the time history of the differenced clock error states estimates and associated $\pm 3\sigma$ bounds for SOP 1 for the INS radio SLAM filter with $n = 2$ known towers and $m = 4$ unknown towers. Pseudoranges were extracted from SOP 1's 3G signals by the on-board receiver for the entirety of flight Run 1.

Fig. 6 also shows the 6 cellular 3G SOP towers' true positions as well as the SOP-INS radio SLAM filter's initial and final estimates of the towers' positions along with the associated horizontal covariances depicted in the form of 95% uncertainty 2–D ellipses in the North-East plane.

Fig. 7 shows the SOP-INS radio SLAM EKF plots for the aircraft's states for two SOP-INS radio SLAM filters: (i) an EKF with knowledge of all the towers' positions ($n = 6$, $m = 0$) and (ii) an EKF with 2 known SOP positions while estimating the positions of the remaining 4 SOPs ($n = 2$, $m = 4$). The altimeter-INS filter errors are not plotted for clarity but the associated $\pm 3\sigma$ bounds are representative of the performance. It is worth noting that the roll angle errors slightly fall outside the $\pm 3\sigma$ bounds for the majority of the flight run. This is suspected to be caused by a subpar estimation of the gyroscope biases. Figs. 8-9 show the EKF plots for SOP 1's horizontal position and differenced clock error states estimated by the SOP-INS radio SLAM filter with *a priori* knowledge of the positions of 2 SOP towers.

2) Flight Run 2: The flight trajectory for Run 2 consisted of a holding pattern comprising almost 3 complete loops having 2 7-km straight segments connected by two 180° banking turns over 6 km. The aircraft flew a 72.7-km trajectory in 12.9 minutes at an average AGL altitude of 5,906 ft and an average speed of 337.4 km/h over an urban region as summarized in Table I. The receiver on-board the aircraft extracted pseudorange measurements from 6 cellular 3G SOPs, 3 of which were available for the entirety of the flight while the remaining 3 SOPs were exploited for 2, 4.3, and 5.5 minutes only. The minimum and maximum distances from the aircarft to any cellular SOP tower over the trajectory were 2.16 and 26.37 km, respectively, and the average distance from the aircraft to the towers ranged from 4.97 to 22.59 km for the closest and furthest towers, respectively. The 3G pseudorange

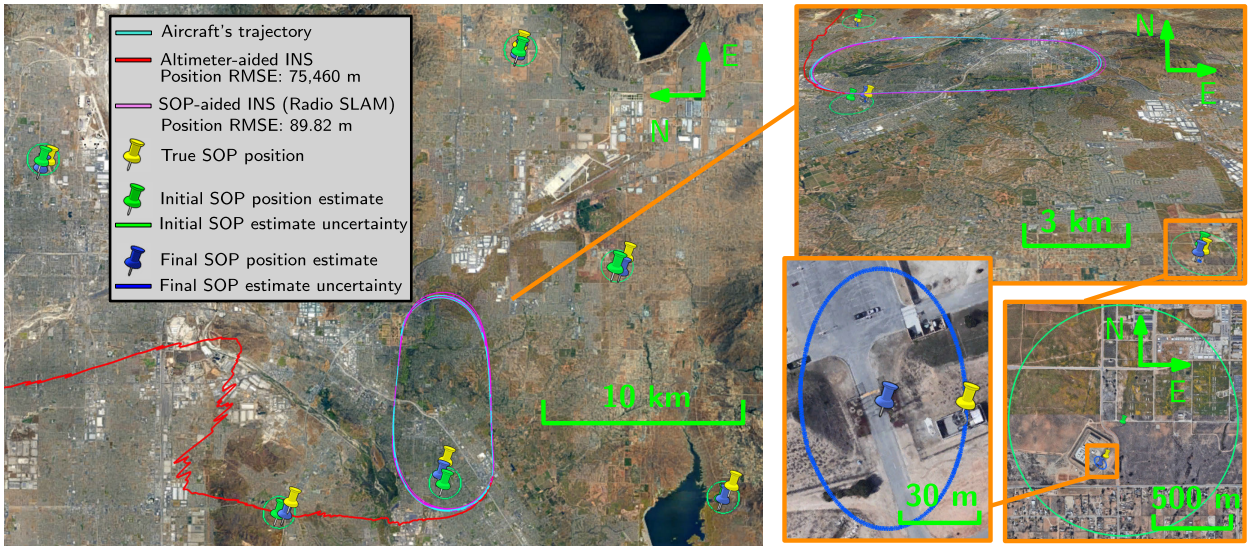

Fig. 10. Left: Flight Run 2 aircraft's true (cyan) and estimated trajectories: (i) SOP-INS radio SLAM with all 6 SOPs unknown (magenta) and (ii) altimeter-aided INS (red). Right: The initial SOP position estimate (green pin) has a 2–D error of 298.98 m (in the North-Eath plane) with respect to the true SOP position (yellow pin) while the final SOP position estimate (blue pin) converged to within 29.54 m from the actual tower after performing radio SLAM for SOP 6. Map data: Google Earth.

TABLE V
FLIGHT RUN 2 EXPERIMENTAL RESULTS

	Altimeter-INS	**Radio SLAM** ($n = 0$, $m = 6$)	**Radio SLAM** ($n = 2$, $m = 4$)	**Radio SLAM** ($n = 6$, $m = 0$)
Attitude RMSE (°)	151.60	4.47	4.43	4.33
Final Att. Error (°)	196.77	3.24	2.70	2.65
Max. Att. Error (°)	299.76	13.81	13.82	13.76
Position RMSE (m)	75,460	89.82 (79.44)	50.24 (55.15)	16.97 (14.20)
Final Pos. Error (m)	141,926	30.85 (50.81)	32.28 (22.47)	8.10 (7.77)
Max. Pos. Error (m)	141,926	214.84 (149.15)	132.62 (179.50)	44.31 (41.43)
Velocity RMSE (m/s)	361.62	0.90 (0.98)	0.65 (0.78)	0.36 (0.53)
Final Vel. Error (m/s)	294.17	0.61 (0.48)	0.17 (0.15)	0.08 (0.14)
Max. Vel. Error (m/s)	627.17	2.36 (3.05)	1.93 (3.61)	1.49 (3.03)

measurement noise variances σ_ρ^2 for flight Run 2 varied between 0.003 m^2 and 0.87 m^2.

Table V summarizes flight Run 2's navigation performance of the altimeter-INS filter and the SOP-INS, and WPA (in parentheses) radio SLAM frameworks with varying levels of *a priori* knowledge on the SOP towers' true positions.

Fig. 10 shows the aircraft's true trajectory, altimeter-INS trajectory, and SOP-INS radio SLAM (with $n = 0$ known towers and $m = 6$ unknown towers) trajectory for flight Run 2. Fig. 10 also shows the 6 3G SOP towers' true positions as well as the SOP-INS radio SLAM filter's initial and final estimates of the towers' positions along with the associated horizontal covariances depicted in the form of 95% uncertainty 2–D ellipses in the North-East plane.

Fig. 11 shows the SOP-INS radio SLAM EKF plots for the aircraft's states for two SOP-INS radio SLAM filters: (i) an EKF with knowledge of all the towers' positions ($n = 6$, $m = 0$) and (ii) an EKF with 2 SOP positions known while estimating the positions of the remaining 4 SOPs ($n = 2$, $m = 4$). The altimeter-INS filter errors are not plotted for clarity but the associated $\pm 3\sigma$ bounds are representative of the performance. Figs. 12-13 show the EKF plots for SOP 4's horizontal position and differenced clock error states estimated by the SOP-INS radio SLAM filter with *a priori* knowledge of the positions of 2 SOP towers.

C. Radio SLAM With Dynamics Model

An EKF was implemented to perform radio SLAM by fusing pseudorange measurements extracted from ambient cellular SOPs in tandem with a WPA dynamics model for EKF time update. The sampling interval T was set to 0.1 s and the updates were also performed at a rate of 10 Hz. The experimental navigation results for flight runs 3 and 4 are presented next.

1) Flight Run 3: The flight trajectory for Run 3 consisted of a descending teardrop maneuver comprising 5 "teardrop" shapes of 20 km each, on average. The teardrop tips passed over the same point in the North-East plane but at different altitudes, with 3 teardrops on one side of the point of interest and 2 on the other side. The aircraft flew a 111.9-km trajectory in 20 minutes at an altitude going from 3,709 to 6,234 ft AGL and an average speed of 335.5 km/h over a semi-urban region as summarized in Table I. The receiver on-board the aircraft intermittently extracted pseudorange measurements from 18 LTE SOP towers. The minimum and maximum distances from the aircraft to any actively used SOP tower over the trajectory were 0.54 and 22.74 km, respectively, and

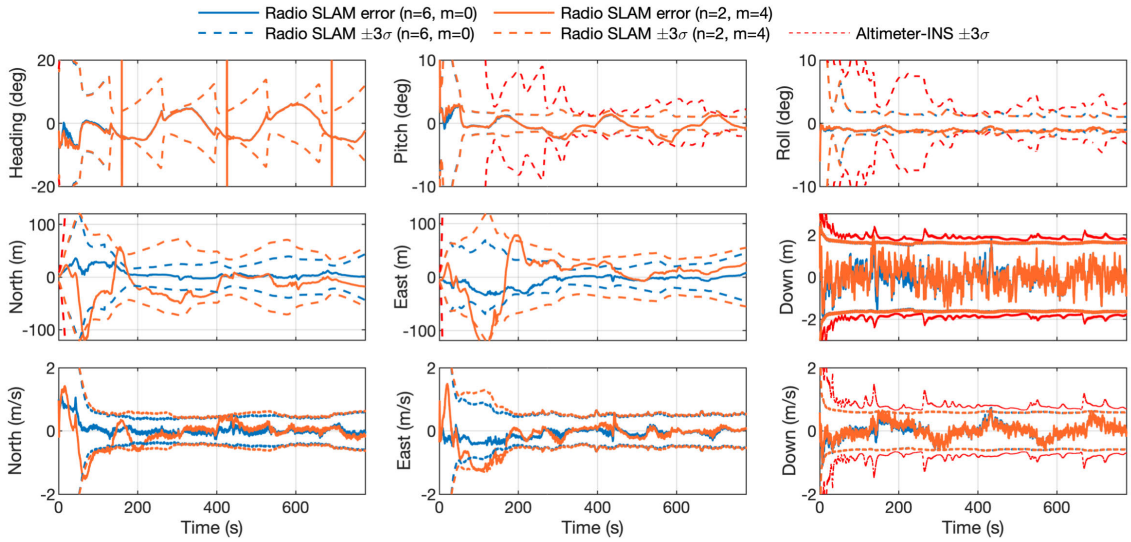

Fig. 11. EKF plots of the time history of the aircraft's states estimation errors and associated $\pm 3\sigma$ bounds for a filter implementing the INS radio SLAM framework on flight run 2 with $n = 6$ known towers and $m = 0$ unknown towers (blue) and $n = 2$ known towers and m=4 unknown towers (orange) as well as the $\pm 3\sigma$ bounds for an altimeter-INS filter (red). The first row corresponds to the orientation states of the aircraft's body frame with respect to the NED frame represented using Euler angles. The second and third rows correspond to the aircraft's position and velocity states in the NED frame, respectively.

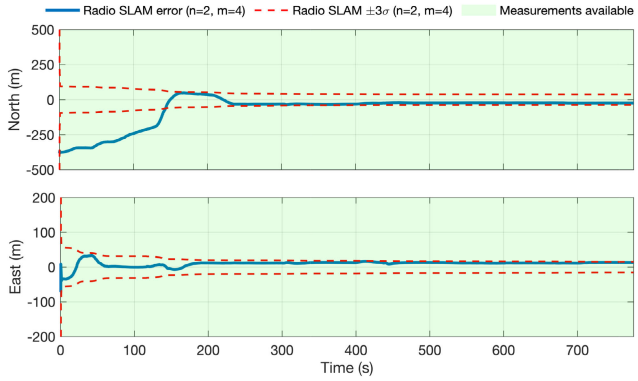

Fig. 12. Flight Run 2 EKF plots of the time history of the horizontal position estimation errors in the North-East plane and associated $\pm 3\sigma$ bounds for SOP 4 for the INS radio SLAM filter with $n = 2$ known towers and $m = 4$ unknown towers. Pseudoranges were extracted from SOP 4's 3G signals by the on-board receiver for the entirety of flight Run 2.

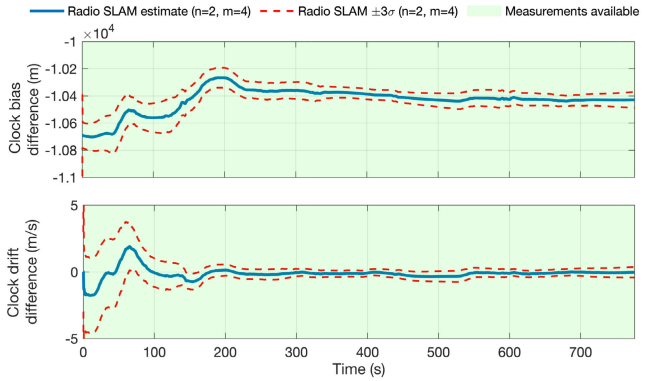

Fig. 13. Flight Run 2 EKF plots of the time history of the differenced clock error states estimates and associated $\pm 3\sigma$ bounds for SOP 4 for the INS radio SLAM filter with $n = 2$ known towers and $m = 4$ unknown towers. Pseudoranges were extracted from SOP 4's 3G signals by the on-board receiver for the entirety of flight Run 2.

the average distance from the aircraft to the tower ranged from 4.71 to 20.25 km for the closest and furthest towers, respectively. The LTE pseudorange measurement noise variances σ_ρ^2 for flight run 3 varied between 0.006 m^2 and 16.81 m^2.

Table VI summarizes flight Run 3's navigation performance of the acceleration random walk radio SLAM framework with varying levels of *a priori* knowledge on the SOP towers' true positions.

Fig. 14 shows the aircraft's true trajectory and radio SLAM (with $n = 0$ known towers and $m = 18$ unknown towers) trajectory for flight Run 3. Fig. 14 also shows the 18 LTE towers' true positions as well as the radio SLAM filter's initial and final estimates of the 18 towers' positions along with the associated horizontal covariances depicted in the form of 95% uncertainty 2–D ellipses in the North-East plane.

Fig. 15 shows the radio SLAM EKF plots for the aircraft's states for two filters: (i) an EKF with knowledge of all the towers' positions ($n = 18$, $m = 0$) and (ii) an EKF with 2 SOP positions known while estimating the positions of the remaining 16 SOPs ($n = 2$, $m = 16$). Figs. 16-17 show the EKF plots for SOP 15's horizontal position and differenced

TABLE VI
FLIGHT RUN 3 EXPERIMENTAL RESULTS

	Radio SLAM ($n = 0$, $m = 18$)	**Radio SLAM** ($n = 2$, $m = 16$)	**Radio SLAM** ($n = 9$, $m = 9$)	**Radio SLAM** ($n = 18$, $m = 0$)
Position RMSE (m)	36.42	26.32	19.15	18.62
Final Pos. Error (m)	16.07	6.29	4.59	3.34
Max. Pos. Error (m)	100.21	88.01	59.16	84.63
Velocity RMSE (m/s)	1.04	1.05	1.03	1.06
Final Vel. Error (m/s)	1.09	1.00	1.02	1.03
Max. Vel. Error (m/s)	3.90	3.90	3.94	3.83

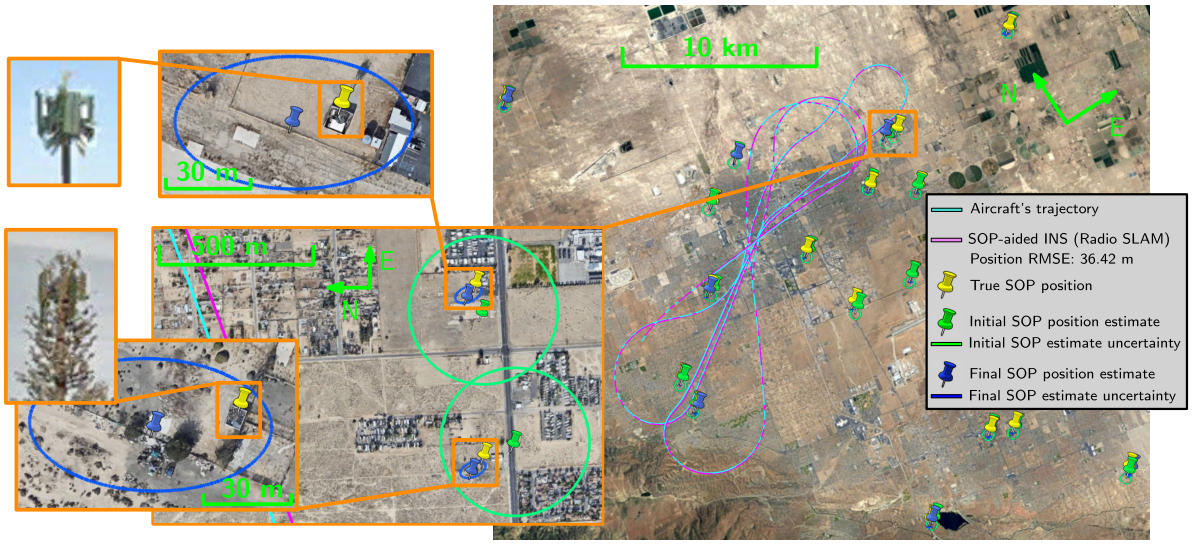

Fig. 14. Flight run 3 aircraft's true (cyan) and estimated WPA radio SLAM trajectory with all 18 SOPs unknown (magenta). The initial SOP position estimates (green pins) have a 134.57 and 71.14 m 2–D error (in the North-Eath plane) with respect to the true SOP positions (yellow pins) while the final SOP position estimates (blue pins) converged to 31.02 and 17.59 m in 2–D error from the actual towers after performing radio SLAM for SOP 1 (bottom) and SOP 11 (top), respectively. Map data: Google Earth.

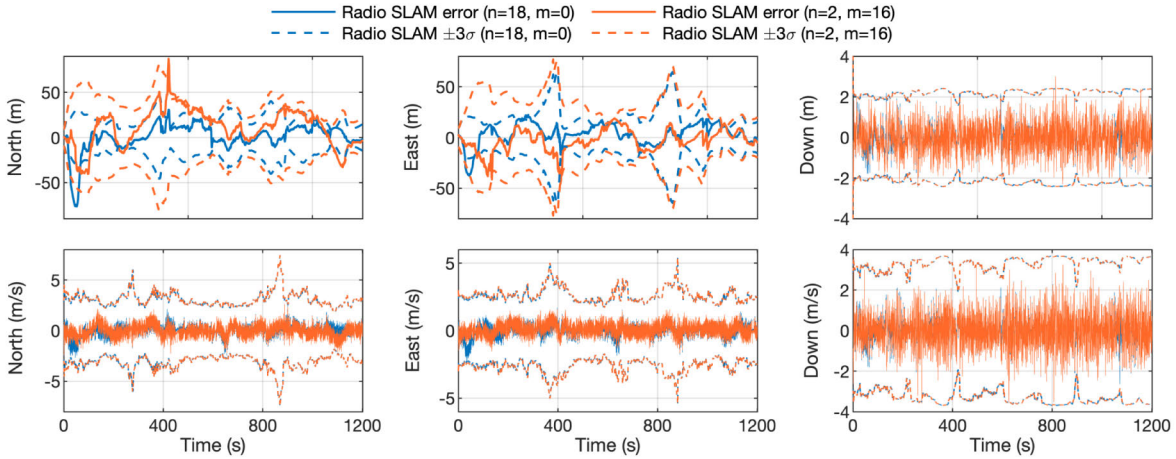

Fig. 15. EKF plots of the time history of the aircraft's states estimation errors and associated $\pm 3\sigma$ bounds for a filter implementing the acceleration randow walk radio SLAM framework on flight run 3 with n=18 known towers and m=0 unknown towers (blue) and n=2 known towers and m=16 unknown towers (orange). The first and second rows correspond to the aircraft's position and velocity states in the NED frame, respectively.

clock error states estimated by the radio SLAM filter with *a priori* knowledge of the positions of 2 SOP towers.

2) Flight Run 4: The flight trajectory for Run 4 consisted of part of a grid maneuver comprising: (i) a 180° banking turn over 10 km, (ii) a 25-km straight segment, (iii) a 270° banking turn over 13 km, (iv) a 23-km straight segment, and (v) a 90° banking turn over 7 km. The aircraft flew a 78.4-km trajectory in 13.8 minutes at an altitude going from 6,234 to 7,546 ft AGL and average speed of 340.1 km/h over a rural region as summarized in Table I. The receiver on-board the aircraft intermittently extracted pseudorange measurements from 32 LTE SOP towers. The minimum and maximum distances from the aircraft to any actively used SOP tower over the trajectory were 4.49 and 108.91 km, respectively, and the average distance from the aircraft to the towers ranged from 12.98 to 98.26 km for the closest and furthest towers, respectively. The LTE pseudorange measurement noise variances σ_ρ^2 for flight run 4 varied between 0.023 m^2 and 20.06 m^2.

TABLE VII
FLIGHT RUN 4 EXPERIMENTAL RESULTS

	Radio SLAM ($n = 0$, $m = 32$)	**Radio SLAM** ($n = 2$, $m = 30$)	**Radio SLAM** ($n = 16$, $m = 16$)	**Radio SLAM** ($n = 32$, $m = 0$)
Position RMSE (m)	67.01	46.34	30.49	25.65
Final Pos. Error (m)	89.60	54.68	21.92	25.50
Max. Pos. Error (m)	121.88	83.54	52.94	50.17
Velocity RMSE (m/s)	0.99	0.93	0.92	0.89
Final Vel. Error (m/s)	0.65	0.57	0.55	0.55
Max. Vel. Error (m/s)	4.72	4.72	4.73	4.75

Table VII summarizes flight Run 4's navigation performance of the acceleration random walk radio SLAM framework with varying levels of *a priori* knowledge on the SOP towers' true positions.

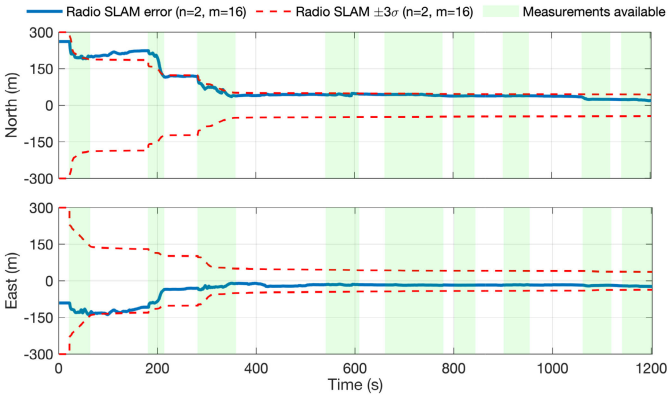

Fig. 16. Flight Run 3 EKF plots of the time history of the horizontal position estimation errors in the North-East plane and associated $\pm 3\sigma$ bounds for SOP 15 for the radio SLAM filter with $n = 2$ known towers and $m = 16$ unknown towers. Pseudoranges were intermittently extracted from SOP 15's LTE signals by the on-board receiver for 547 seconds out of the 1201 seconds.

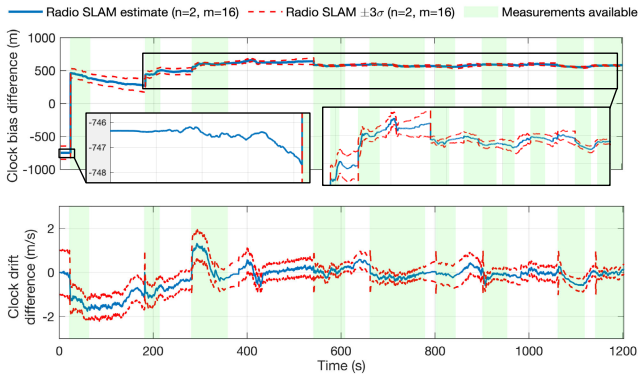

Fig. 17. Flight Run 3 EKF plots of the time history of the differenced clock error states estimates and associated $\pm 3\sigma$ bounds for SOP 15 for the radio SLAM filter with $n = 2$ known towers and $m = 16$ unknown towers. Pseudoranges were intermittently extracted from SOP 15's LTE signals by the on-board receiver for 547 seconds out of the 1201 seconds.

Fig. 18 shows the aircraft's true trajectory and radio SLAM (with $n = 0$ known towers and $m = 32$ unknown towers) trajectory for flight Run 4. Fig. 18 also shows the 32 LTE SOP towers' true positions as well as the radio SLAM filter's initial and final estimates of the towers' positions along with the associated horizontal covariances depicted in the form of 95% uncertainty 2–D ellipses in the North-East plane.

Fig. 19 shows the radio SLAM EKF plots for the aircraft's states for two radio SLAM filters: (i) an EKF with knowledge of all the towers positions ($n = 32$, $m = 0$) and (ii) an EKF with 2 SOP positions known while estimating the positions of the remaining 30 SOPs ($n = 2$, $m = 30$). Figs. 20-21 show the EKF plots for SOP 27's horizontal position and differenced clock error states estimated by the radio SLAM filter with *a priori* knowledge of the positions of 2 SOP towers.

D. Discussion

The following observations and conclusions can be drawn from previous results.

- As can be seen in Figs. 7-11 and 15-19, the aircraft's states EKF plots are similar and offer the same patterns for different levels of SOP position knowledge across the 4 different flight runs. This is on one hand explained by the fact that the estimated states are initialized with the same error for all EKF radio SLAM filters processing each run. On the other hand, there is no significant differences in the geometry between the SOP towers and the aircraft over the course of the flight runs: the unit line-of-sight (LOS) vector pointing from the SOPs to the aircraft is very similar between filters with different *a priori* SOP position knowledge as the initial tower position uncertainty is negligible compared to the distances between the aircraft and the SOPs. The covariances are, however, always bigger for filters with less *a priori* SOP position knowledge as more information yields tighter $\pm 3\sigma$ bounds in the aircraft's states EKF plots.
- The orientation states errors and associated uncertainties are observed to be very similar between different radio SLAM filters with varying *a priori* information, suggesting that SOP position information does not significantly affect orientation estimation.
- It is interesting to note the spikes in heading error in Figs. 7-11, with one occurring for flight run 1 and three occurring for flight run 2. These spikes are actually resulting from singularities in the ground truth orientation reported in Euler angles. The formulation of the INS radio SLAM EKF filter with quaternion states to estimate the aircraft's orientation was chosen to circumvent this specific issue as detailed in Subection III-A.
- It is important to note that a filter not exploiting ambient cellular SOPs opportunistically and aiding the INS with altimeter measurements only diverges as shown in Figs. 6-10. This is also revealed in the aircraft's EKF plots in Figs. 7-11 with diverging bounds in the North and East position and velocity states, looser bounds on orientation (heading in particular) as compared to a radio SLAM filter while the altimeter measurements prevent the Down states from diverging.
- It is worth noting that the intermittency of LTE pseudoranges in flight runs 3 and 4, as can be seen in the various measurement availability periods in Figs. 16-17 and 20-21, requires clock error states reinitialization when the measurements are available from an SOP after a period of unavailability. This reinitialization is revealed by the jump in clock errors states estimates as well as spike in the associated covariance preceding every period of measurement availability in Figs. 17-21. This reinitialization of clock error states, essential to accomodate intermittent measurements, hampers the radio SLAM EKF performance and explains the lower initial uncertainty around SOP positions in flight runs 3 and 4 as compared to runs 1 and 2 where measurements are continuous.
- The differenced clock error states get updated even before the first period of availability of measurements as can be seen in SOP 15's clock states EKF plots in Fig. 17. This is expected as these differenced states contain the receiver clock error states, which are also present in all other SOPs' clock differenced states. These common terms result in correlations between the SOPs' clock error states that in turn yield updates for SOP clock states even when

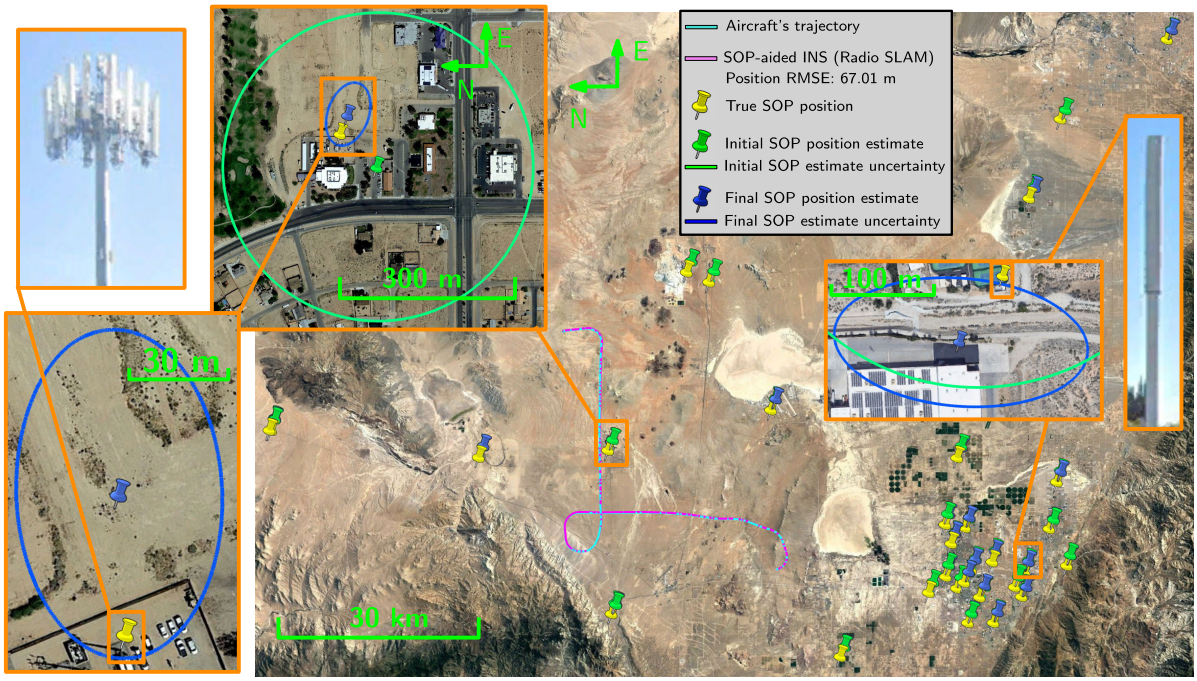

Fig. 18. Flight run 4 aircraft's true (cyan) and WPA radio SLAM trajectory with all (32) SOPs unknown (magenta). The initial SOP position estimates (green pins) have a 139.29 and 74.80 m 2–D error (in the North-Eath plane) with respect to the true SOP positions (yellow pins) while the final SOP position estimates (blue pins) converged to 75.19 and 50.40 m in 2–D error from the actual towers after performing radio SLAM for SOP 23 (right) and SOP 27 (left), respectively. Map data: Google Earth.

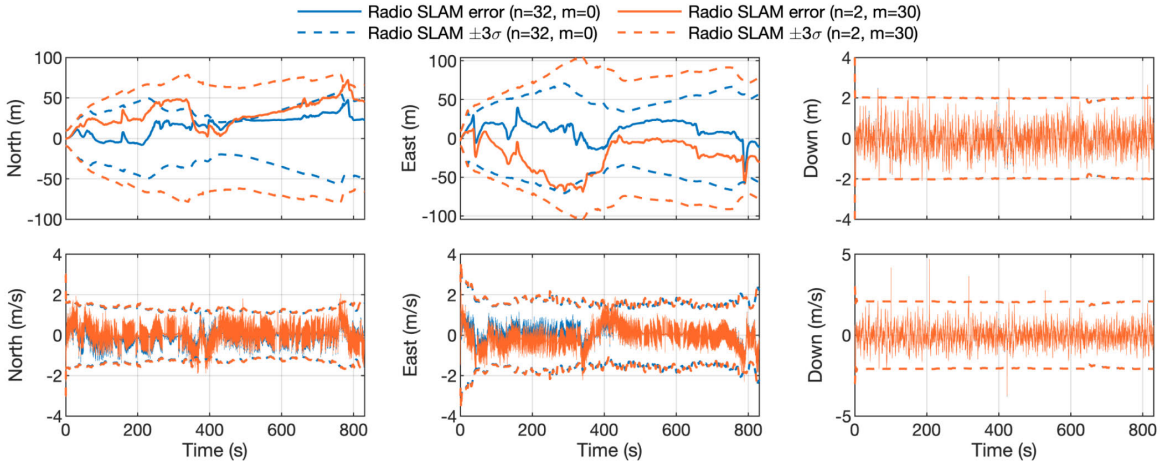

Fig. 19. EKF plots of the time history of the aircraft's states estimation errors and associated $\pm 3\sigma$ bounds for a filter implementing the acceleration randow walk radio SLAM framework on flight run 4 with n=32 known towers and m=0 unknown towers (blue) and n=2 known towers and m=30 unknown towers (orange). The first and second rows correspond to the aircraft's position and velocity states in the NED frame, respectively.

measurements from the SOP associated to these clock states are not available (provided measurements from at least one other SOP are available at that time).

- SOP 15's position states do not get updated before the first period of measurement availability as expected and as can be seen in Fig. 16. However, after the first interval of measurement availability for SOP 15, it is interesting to note that the positions states of this SOP get updated even when no measurements are available for SOP 15. This is explained by the fact that cross-correlations are built in the estimation error covariance matrix during the EKF update step between states of active SOPs. These cross-correlations then result in updates to SOP position states even when no measurements are available from the SOP associated with these states.
- The estimation performance degrades as the navigating receiver's *a priori* knowledge of the SOP towers positions decreases (i.e., as the number of unknown SOPs increases). This is observed across all 4 flight runs and with both INS and WPA radio SLAM frameworks as summarized in Tables IV-VII. Additionally, no noticeable or significant differences were observed in the measurement quality and/or estimation performance across the various environments (rural, semi-urban, and urban). The readers are referred [59] for a detailed analysis of the cellular SOP signals extracted opportunistically at aircraft altitudes across the different environments.
- The direct comparison of both radio SLAM frameworks, with the INS and with the WPA model as the tools used in the EKF propagation step, was performed for

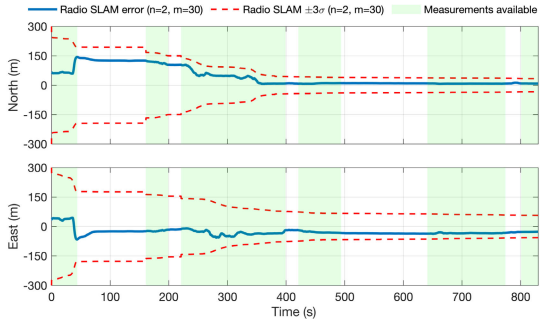

Fig. 20. Flight Run 4 EKF plots of the time history of the horizontal position estimation errors in the North-East plane and associated $\pm 3\sigma$ bounds for SOP 27 for the radio SLAM filter with $n = 2$ known towers and $m = 30$ unknown towers. Pseudoranges were intermittently extracted from SOP 27's LTE signals by the on-board receiver for 490 seconds out of the 830 seconds.

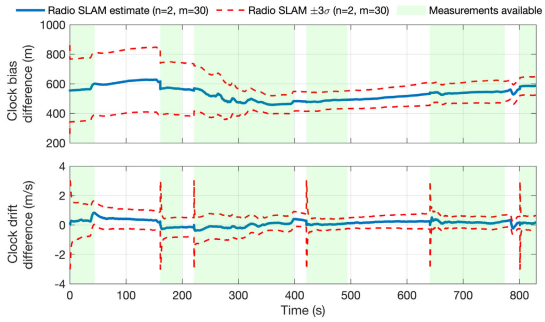

Fig. 21. Flight Run 4 EKF plots of the time history of the differenced clock error states estimates and associated $\pm 3\sigma$ bounds for SOP 27 for the radio SLAM filter on flight run 4 with $n = 2$ known towers and $m = 30$ unknown towers. Pseudoranges were intermittently extracted from SOP 27's LTE signals by the on-board receiver for 490 seconds out of the 830 seconds.

flight runs 1 and 2 where IMU measurements were available as shown in Tables IV-V. It can be observed that the position estimation performance is comparable between both frameworks as the WPA model is able to capture the dynamics of the maneuvers in the position state estimates. The velocity estimation performance is, however, worse for the WPA model than for the INS. This can also be seen from the high-frequency fluctuations in the velocity errors in the aircraft EKF plots in flight runs 3 and 4 (processed with the WPA dynamical model) in Figs. 15-19.

- The nonlinearity of the pseudorange measurements results in local observability of the radio SLAM framework [43]. As a result, initializing the SOP with "too large" uncertainty will lead the EKF to converge to a local minimum, in which the SOP position state estimate converges to an erroneous position. In such a case, the aircraft's navigation solution also converges to an erroneous one as the EKF fits the measurements to the erroneously converged tower positions. The initial SOP position uncertainty was selected empirically to be towards the upper limit of the "allowable" initial uncertainty before the local nonlinear observability issues kick in. Also, note that it is smaller for 4G SOPs than for 3G ones since the 4G pseudoranges are intermittent (and require re-initialization of the clock error states) while the 3G ones are continuous. Determining when the SOP position initialization uncertainty becomes "too large" is an interesting research question and is left as future work.
- Multiple-source (SOP-GNSS-IMU) integrity monitoring should be implemented, considering the safety-critical nature of radio SLAM applied to high-altitude aircraft navigation. Recent studies considered integrity monitoring of SOP-GNSS on UAVs [68], [69] and SOP-GNSS-IMU on ground vehicles [70], but the SOP positions were assumed to be known. A follow-up study for radio SLAM with unknown positions is beyond the scope of this paper and is deferred to future work.

VI. Conclusion

This paper presented an extensive evaluation of radio SLAM to enable aircraft navigation without GNSS signals, by exploiting pseudorange measurements from unknown terrestrial SOPs. Starting with an initial estimate of the aircraft's states, radio SLAM estimates the states of the aircraft simultaneously with the SOPs' states. Two radio SLAM frameworks were studied: (i) tightly-coupled SOP-aided INS and (ii) utilizing a WPA dynamical model for the aircraft's dynamics instead of the INS. Results from four flight runs on a USAF C-12 aircraft, equipped with an altimeter and an industrial-grade IMU, were presented. Different *a priori* conditions of the SOPs' positions were studied. The results consistently demonstrated the promise of real-world aircraft navigation via radio SLAM, yielding bounded errors along trajectories of tens of kilometers, with potentially meter-level navigation accuracy. Future work should study the achievable performance and its repeatability to satisfy minimum operational performance standards (MOPS).

Appendix A
EKF Time Update of $\boldsymbol{x}_{\mathrm{r,ins}}$

The time update of $\boldsymbol{x}_{\mathrm{r,ins}}$ is performed using strapdown INS mechanization equations in the ECEF frame $\{e\}$ when IMU measurements are available [61], [62].

A. Orientation Time Update

The orientation time update is given by

$$ {}^{b}_{e}\hat{\bar{\boldsymbol{q}}}(k+1|j) = {}^{b_{k+1}}_{b_k}\hat{\bar{\boldsymbol{q}}} * {}^{b}_{e}\hat{\bar{\boldsymbol{q}}}(k|j), \tag{15} $$

where ${}^{b_{k+1}}_{b_k}\hat{\bar{\boldsymbol{q}}}$ represents an estimate of the rotation quaternion between the IMU's body frame at time k and $k+1$ and $*$ denotes the quaternion product. The quaternion ${}^{b_{k+1}}_{b_k}\hat{\bar{\boldsymbol{q}}}$ is computed by integrating gyroscope rotation rate data $\boldsymbol{\omega}_{\mathrm{imu}}(k)$ and $\boldsymbol{\omega}_{\mathrm{imu}}(k+1)$ using a fourth-order Runge-Kutta according to

$$ {}^{b_{k+1}}_{b_k}\hat{\bar{\boldsymbol{q}}} = \bar{\boldsymbol{q}}_0 + \frac{T}{6}\left(\boldsymbol{d}_1 + 2\boldsymbol{d}_2 + 2\boldsymbol{d}_3 + \boldsymbol{d}_4\right), $$

where

$$ \boldsymbol{d}_1 = \frac{1}{2}\boldsymbol{\Omega}\left[{}^{b}\hat{\boldsymbol{\omega}}(k)\right]\cdot\bar{\boldsymbol{q}}_0, \quad \boldsymbol{d}_2 = \frac{1}{2}\boldsymbol{\Omega}\left[\bar{\boldsymbol{\omega}}\right]\cdot\left(\bar{\boldsymbol{q}}_0 + \frac{1}{2}T\boldsymbol{d}_1\right), $$

$$ \boldsymbol{d}_3 = \frac{1}{2}\boldsymbol{\Omega}\left[\bar{\boldsymbol{\omega}}\right]\cdot\left(\bar{\boldsymbol{q}}_0 + \frac{1}{2}T\boldsymbol{d}_2\right), $$

$$ \boldsymbol{d}_4 = \frac{1}{2}\boldsymbol{\Omega}\left[{}^{b}\hat{\boldsymbol{\omega}}(k+1)\right]\cdot\left(\bar{\boldsymbol{q}}_0 + T\boldsymbol{d}_3\right), \quad \bar{\boldsymbol{q}}_0 \triangleq [\,0,\,0,\,0,\,1\,]^{\mathsf{T}}, $$

$$ \bar{\boldsymbol{\omega}} \triangleq \frac{1}{2}\left[{}^{b}\hat{\boldsymbol{\omega}}(k) + {}^{b}\hat{\boldsymbol{\omega}}(k+1)\right] - {}^{e}_{b}\mathbf{R}^{\mathsf{T}}(k)\,{}^{e}_{i}\boldsymbol{\omega}, $$

where $\boldsymbol{\Omega}[\,\cdot\,] \in \mathbb{R}^{4\times4}$ is given by

$$\boldsymbol{\Omega}[\boldsymbol{a}] \triangleq \begin{bmatrix} -\lfloor \boldsymbol{a}\times \rfloor & \boldsymbol{a} \\ -\boldsymbol{a}^{\mathsf{T}} & 0 \end{bmatrix}, \quad \boldsymbol{a} \triangleq [a_1, a_2, a_3]^{\mathsf{T}},$$

$\lfloor \boldsymbol{a}\times \rfloor \in \mathbb{R}^{3\times3}$ is the skew-symmetric matrix form of $\boldsymbol{a}$ and is found by

$$\lfloor \boldsymbol{a}\times \rfloor \triangleq \begin{bmatrix} 0 & -a_3 & a_2 \\ a_3 & 0 & -a_1 \\ -a_2 & a_1 & 0 \end{bmatrix},$$

${}^{b}\hat{\boldsymbol{\omega}}(k)$ is the bias-compensated rotation rate measurement, which is computed according to

$${}^{b}\hat{\boldsymbol{\omega}}(k) = \boldsymbol{\omega}_{\text{imu}}(k) - \hat{\boldsymbol{b}}_{\text{gyr}}(k|j), \tag{16}$$

and ${}^{e}_{i}\boldsymbol{\omega} \triangleq \left[0, 0, {}^{e}_{i}\omega\right]^{\mathsf{T}}$ is the rotation rate of Earth, i.e., the rotation rate of the ECEF frame $\{e\}$ with respect to the ECI frame $\{i\}$. The value of ${}^{e}_{i}\omega$ is 7.292115×10^{-5} rad/s according to the latest version of the World Geodetic System (WGS84).

B. Velocity and Position Time Update

IMU specific force measurements are integrated using trapezoidal integration to perform a time update of the position and velocity in the ECEF coordinate frame while accounting for the Coriolis effect introduced by the rotation rate of Earth ${}^{e}_{i}\boldsymbol{\omega}$ [62]. Assuming that the variation of the Coriolis force is negligible over the integration interval, the velocity time update is performed as

$$\begin{aligned} {}^{e}\hat{\boldsymbol{r}}_b(k+1|j) &= {}^{e}\hat{\boldsymbol{r}}_b(k|j) + \frac{T}{2}\left[{}^{e}\hat{\boldsymbol{a}}(k) + {}^{e}\hat{\boldsymbol{a}}(k+1)\right] \\ &\quad + {}^{e}\boldsymbol{g}({}^{e}\boldsymbol{r}_b(k))T - 2T\lfloor {}^{e}_{i}\boldsymbol{\omega}\times\rfloor {}^{e}\hat{\dot{\boldsymbol{r}}}_b(k|j), \end{aligned} \tag{17}$$

where ${}^{e}\hat{\boldsymbol{a}}$ and ${}^{b}\hat{\boldsymbol{a}}$ are the transformed bias-compensated specific force and untransformed bias-compensated specific force, respectively, which are given by

$${}^{e}\hat{\boldsymbol{a}}(k) \triangleq \hat{\mathbf{R}}^{\mathsf{T}}(k)\,{}^{b}\hat{\boldsymbol{a}}(k), \tag{18}$$

$${}^{b}\hat{\boldsymbol{a}}(k) = \hat{\boldsymbol{a}}_{\text{imu}}(k) - \hat{\boldsymbol{b}}_{\text{acc}}(k|j), \tag{19}$$

and $\hat{\mathbf{R}}(k) \triangleq \mathbf{R}\left[{}^{b}_{e}\hat{\boldsymbol{q}}(k|j)\right]$ is the rotation matrix from frame $\{e\}$ to frame $\{b\}$ associated with the quaternion ${}^{b}_{e}\hat{\boldsymbol{q}}(k|j)$.

The position time update is performed according to

$$\begin{aligned} {}^{e}\hat{\boldsymbol{r}}_b(k+1|j) &= {}^{e}\hat{\boldsymbol{r}}_b(k|j) + \frac{T}{2}\left[{}^{e}\hat{\dot{\boldsymbol{r}}}_b(k|j) + {}^{e}\hat{\dot{\boldsymbol{r}}}(k+1|j)\right] \\ &\quad - T^2\lfloor {}^{e}_{i}\boldsymbol{\omega}\times\rfloor {}^{e}\hat{\dot{\boldsymbol{r}}}_b(k|j). \end{aligned} \tag{20}$$

APPENDIX B
INS STATE TRANSITION AND PROCESS NOISE COVARIANCE MATRICES

The calculation of the discrete-time linearized INS state transition matrix $\boldsymbol{\Phi}_{\text{ins}}$ and process noise covariance $\mathbf{Q}_{\text{ins}}$ are performed using strapdown INS equations as described in [61] and [62]. The discrete-time linearized INS state transition matrix $\boldsymbol{\Phi}_{\text{ins}}$ is given by

$$\boldsymbol{\Phi}_{\text{ins}} = \begin{bmatrix} \boldsymbol{\Phi}_{\boldsymbol{qq}} & \mathbf{0}_{3\times3} & \mathbf{0}_{3\times3} & \boldsymbol{\Phi}_{\boldsymbol{q}\boldsymbol{b}_{\text{gyr}}} & \mathbf{0}_{3\times3} \\ \boldsymbol{\Phi}_{\boldsymbol{rq}} & \mathbf{I}_{3\times3} & T\mathbf{I}_{3\times3} & \boldsymbol{\Phi}_{\boldsymbol{r}\boldsymbol{b}_{\text{gyr}}} & \boldsymbol{\Phi}_{\boldsymbol{r}\boldsymbol{b}_{\text{acc}}} \\ \boldsymbol{\Phi}_{\dot{\boldsymbol{r}}\boldsymbol{q}} & \mathbf{0}_{3\times3} & \boldsymbol{\Phi}_{\dot{\boldsymbol{r}}\dot{\boldsymbol{r}}} & \boldsymbol{\Phi}_{\dot{\boldsymbol{r}}\boldsymbol{b}_{\text{gyr}}} & \boldsymbol{\Phi}_{\dot{\boldsymbol{r}}\boldsymbol{b}_{\text{acc}}} \\ \mathbf{0}_{3\times3} & \mathbf{0}_{3\times3} & \mathbf{0}_{3\times3} & \mathbf{I}_{3\times3} & \mathbf{0}_{3\times3} \\ \mathbf{0}_{3\times3} & \mathbf{0}_{3\times3} & \mathbf{0}_{3\times3} & \mathbf{0}_{3\times3} & \mathbf{I}_{3\times3} \end{bmatrix},$$

where

$$\begin{aligned} &\boldsymbol{\Phi}_{\boldsymbol{qq}} = \mathbf{I}_{3\times3} - T\lfloor {}^{e}_{i}\boldsymbol{\omega}\times\rfloor, \quad \boldsymbol{\Phi}_{\dot{\boldsymbol{r}}\dot{\boldsymbol{r}}} = \mathbf{I}_{3\times3} - 2T\lfloor {}^{e}_{i}\boldsymbol{\omega}\times\rfloor, \\ &\boldsymbol{\Phi}_{\boldsymbol{q}\boldsymbol{b}_{\text{gyr}}} = -\frac{T}{2}\left[\hat{\mathbf{R}}^{\mathsf{T}}(k) + \hat{\mathbf{R}}^{\mathsf{T}}(k+1)\right], \\ &\boldsymbol{\Phi}_{\dot{\boldsymbol{r}}\boldsymbol{q}} = -\frac{T}{2}\left\lfloor\left[{}^{e}\hat{\boldsymbol{a}}(k) + {}^{e}\hat{\boldsymbol{a}}(k+1)\right]\times\right\rfloor, \quad \boldsymbol{\Phi}_{\boldsymbol{rq}} = \frac{T}{2}\boldsymbol{\Phi}_{\dot{\boldsymbol{r}}\boldsymbol{q}}, \\ &\boldsymbol{\Phi}_{\dot{\boldsymbol{r}}\boldsymbol{b}_{\text{gyr}}} = -\frac{T}{2}\left\lfloor {}^{e}\hat{\boldsymbol{a}}(k)\times\right\rfloor \boldsymbol{\Phi}_{\boldsymbol{q}\boldsymbol{b}_{\text{gyr}}}, \quad \boldsymbol{\Phi}_{\dot{\boldsymbol{r}}\boldsymbol{b}_{\text{acc}}} = \boldsymbol{\Phi}_{\boldsymbol{q}\boldsymbol{b}_{\text{gyr}}}, \\ &\boldsymbol{\Phi}_{\boldsymbol{r}\boldsymbol{b}_{\text{gyr}}} = \frac{T}{2}\boldsymbol{\Phi}_{\dot{\boldsymbol{r}}\boldsymbol{b}_{\text{gyr}}}, \quad \boldsymbol{\Phi}_{\boldsymbol{r}\boldsymbol{b}_{\text{acc}}} = \frac{T}{2}\boldsymbol{\Phi}_{\dot{\boldsymbol{r}}\boldsymbol{b}_{\text{acc}}}. \end{aligned}$$

The discrete-time linearized INS process noise covariance $\mathbf{Q}_{\text{ins}}$ is given by

$$\mathbf{Q}_{\text{ins}} = \frac{T}{2}\left(\boldsymbol{\Phi}_{\text{ins}}\mathbf{N}_c\boldsymbol{\Phi}_{\text{ins}}^{\mathsf{T}} + \mathbf{N}_c\right),$$

where

$$\mathbf{N}_c = \text{diag}\left[\mathbf{S}_{\text{ng}},\ \mathbf{0}_{3\times3},\ \mathbf{S}_{\text{na}},\ \mathbf{S}_{\text{bg}},\ \mathbf{S}_{\text{ba}}\right],$$

with $\mathbf{S}_{\text{ng}} = T\mathbf{Q}_{\text{ng}}$ and $\mathbf{S}_{\text{na}} = T\mathbf{Q}_{\text{na}}$ are the PSD matrices of the gyroscope's and accelerometer's random noise, respectively, and $\mathbf{S}_{\text{bg}} = \mathbf{Q}_{\text{bg}}/T$ and $\mathbf{S}_{\text{ba}} = \mathbf{Q}_{\text{ba}}/T$ are the PSD matrices of the gyroscope's and accelerometer's bias instability, respectively.

APPENDIX C
EKF MEASUREMENT UPDATE OF $\boldsymbol{x}_{\text{r,ins}}$

The standard EKF equations are modified to deal with the 3–D orientation error correction, which contains one less dimension than the 4–D orientation quaternion estimate, as described in Subsection III-A. To this end, the state estimate is separated into two parts according to $\hat{\boldsymbol{x}}_{\text{ins}} \triangleq \left[{}^{b}_{e}\hat{\boldsymbol{q}}^{\mathsf{T}}, \hat{\boldsymbol{y}}^{\mathsf{T}}\right]^{\mathsf{T}}$, where ${}^{b}_{e}\hat{\boldsymbol{q}} \in \mathbb{R}^4$ is the orientation quaternion estimate and $\hat{\boldsymbol{y}} \in \mathbb{R}^{12+5M}$ is a vector containing the remaining estimates of $\boldsymbol{x}_{\text{ins}}$. Next, the EKF correction vector $\breve{\boldsymbol{x}}_{\text{ins}}(k+1)$, which is to be applied to $\hat{\boldsymbol{x}}_{\text{ins}}(k+1|j)$ to produce the EKF state measurement update $\hat{\boldsymbol{x}}_{\text{ins}}(k+1|k+1)$, is computed and partitioned according to

$$\breve{x}_{\text{ins}}(k+1) = \mathbf{K}(k+1)\boldsymbol{\nu}(k+1|j) \triangleq \begin{bmatrix} \breve{\boldsymbol{\theta}}(k+1) \\ \breve{\boldsymbol{y}}(k+1) \end{bmatrix},$$

where $\mathbf{K}(k+1)$ is the standard Kalman gain, $\boldsymbol{\nu}(k+1|j) \triangleq \boldsymbol{z}(k+1) - \hat{\boldsymbol{z}}(k+1|j)$ is the measurement innovations, $\breve{\boldsymbol{\theta}} \in \mathbb{R}^3$ is the orientation correction, and $\breve{\boldsymbol{y}} \in \mathbb{R}^{12+5M}$ is a vector containing the remaining corrections. Finally, the EKF state measurement update $\hat{\boldsymbol{x}}_{\text{ins}}(k+1|k+1)$ is computed by applying $\breve{\boldsymbol{\theta}}(k+1)$ to ${}^{b}_{e}\hat{\boldsymbol{q}}(k+1|j)$ and $\breve{\boldsymbol{y}}(k+1)$ to $\hat{\boldsymbol{y}}(k+1|j)$ as follows

$$\begin{aligned} &\hat{\boldsymbol{x}}_{\text{ins}}(k+1|k+1) \\ &= \begin{bmatrix} {}^{b}_{e}\hat{\boldsymbol{q}}(k+1|j) * \left[\frac{1}{2}\breve{\boldsymbol{\theta}}^{\mathsf{T}}(k+1), \sqrt{1-\frac{1}{4}\breve{\boldsymbol{\theta}}^{\mathsf{T}}(k+1)\breve{\boldsymbol{\theta}}(k+1)}\right]^{\mathsf{T}} \\ \hat{\boldsymbol{y}}(k+1|j) + \breve{\boldsymbol{y}}(k+1) \end{bmatrix}. \end{aligned}$$

ACKNOWLEDGMENT

The authors would like to thank Edwards AFB and Holloman AFB for inviting the ASPIN Laboratory to conduct the "SNIFFER: Signals of opportunity for Navigation In Frequency-Forbidden EnviRonments" flight campaign. The authors would like to thank Joshua Morales, Kimia Shamaei, Mahdi Maaref, Kyle Semelka, MyLinh Nguyen, and Trier Mortlock for their help with preparing for data collection. The authors would also like to thank Ali Abdallah, Shaghayegh Shahcheraghi, and Ali Kaiss for their help with data processing. DISTRIBUTION STATEMENT A. Approved for public release; Distribution is unlimited. 412TW-PA-20146.

Sandia National Laboratories is a multimission laboratory managed and operated by National Technology & Engineering Solutions of Sandia, LLC, a wholly owned subsidiary of Honeywell International Inc., for the U.S. Department of Energy's National Nuclear Security Administration under contract DE-NA0003525. This paper describes objective technical results and analysis. Any subjective views or opinions that might be expressed in the paper do not necessarily represent the views of the U.S. Department of Energy or the United States Government.

REFERENCES

[1] R. Sabatini et al., "Avionics systems panel research and innovation perspectives," *IEEE Aerosp. Electron. Syst. Mag.*, vol. 35, no. 12, pp. 58–72, Dec. 2020.

[2] J. Lee, S. Pullen, S. Datta-Barua, and J. Lee, "Real-time ionospheric threat adaptation using a space weather prediction for GNSS-based aircraft landing systems," *IEEE Trans. Intell. Transp. Syst.*, vol. 18, no. 7, pp. 1752–1761, Jul. 2017.

[3] O. Osechas, F. Fohlmeister, T. Dautermann, and M. Felux, "Impact of GNSS-band radio interference on operational avionics," *NAVIGATION: J. Inst. Navigat.*, vol. 69, no. 2, pp. 1–9, 2022.

[4] M. Uijt de Haag, E. Dill, S. Young, and M. Joerger, *Position, Navigation, and Timing Technologies in the 21st Century*, vol. 2, J. Morton, F. van Diggelen, J. Spilker Jr., and B. Parkinson, Eds. Hoboken, NJ, USA: Wiley, 2021, ch. 60, pp. 1171–1223.

[5] A. P. Cohen, S. A. Shaheen, and E. M. Farrar, "Urban air mobility: History, ecosystem, market potential, and challenges," *IEEE Trans. Intell. Transp. Syst.*, vol. 22, no. 9, pp. 6074–6087, Sep. 2021.

[6] International Civil Aviation Organization (ICAO). (May 2019). *An Urgent Need to Address Harmful Interferences to GNSS*. [Online]. Available: https://www.iata.org/contentassets/e45e5219cc8c4277a0e80562590793da/address-harmful-interferences-gnss.pdf

[7] International Air Transport Association (IATA), Global Aviation Data Management. (Oct. 2022). *GNSS/GPS Interference Reported in MENA Region Jan-Dec 2021*. [Online]. Available: https://www.icao.int/MID/Documents/2022/SEIG4%20and%20NASP/PPT5.pdf

[8] International Telecommunication Union (ITU). (Jul. 2022). *Prevention of Harmful Interference to Radio Navigation Satellite Service Receivers in the 1559–1610 mhz Frequency Band*. [Online]. Available: https://www.itu.int/dms_pub/itu-r/md/00/cr/cir/R00-CR-CIR-0488!!PDF-E.pdf

[9] EUROCONTROL, Aviation Intelligence Unit. (Mar. 2021). *Does Radio Frequency Interference to Satellite Navigation Pose an Increasing Threat to Network Efficiency, Cost-Effectiveness and Ultimately Safety?* [Online]. Available: https://www.eurocontrol.int/sites/default/files/2021-03/eurocontrol-think-paper-9-radio-frequency-intereference-satellite-navigation.pdf

[10] Z. Liu, S. Lo, and T. Walter. (Aug. 2022). *Protecting GNSS for Safe Aviation*. [Online]. Available: https://insidegnss.com/protecting-gnss-for-safe-aviation

[11] D. Goodin. (Oct. 2022). *GPS Interference Caused the FAA To reroute Texas Air Traffic. Experts Stumped*. [Online]. Available: https://arstechnica.com/information-technology/2022/10/cause-is-unknown-for-mysterious-gps-outage-that-rerouted-texas-air-traffic/

[12] M. Bartock et al., "Foundational PNT profile: Applying the cybersecurity framework for the responsible use of positioning, navigation, and timing (PNT) services," Nat. Inst. Standards Technol. (NIST), Gaithersburg, MD, USA, Tech. Rep. 8323, Feb. 2021.

[13] International Air Transport Association (IATA). (Mar. 2023). *Harmful Interference to Global Navigation Satellite System (GNSS) and Its Impacts on Flight and Air Traffic Management Operations*. [Online]. Available: https://www.iata.org/contentassets/d7e421981aa64169af1a8d6b37438d4d/tib—gnss-interference—20230330.pdf

[14] M. Maaref and Z. Kassas, "Ground vehicle navigation in GNSS-challenged environments using signals of opportunity and a closed-loop map-matching approach," *IEEE Trans. Intell. Transp. Syst.*, vol. 21, no. 7, pp. 2723–2738, Jul. 2020.

[15] J. Raquet et al., *Position, Navigation, and Timing Technologies in the 21st Century*, vol. 2, J. Morton, F. van Diggelen, J. Spilker, Jr., and B. Parkinson, Eds. Hoboken, NJ, USA: Wiley, 2021, ch. 35–43, pp. 1115–1412.

[16] M. M. Rahman, V. Moghtadaiee, and A. G. Dempster, "Design of fingerprinting technique for indoor localization using AM radio signals," in *Proc. Int. Conf. Indoor Positioning Indoor Navigat. (IPIN)*, Sep. 2017, pp. 1–7.

[17] X. Chen, Q. Wei, F. Wang, Z. Jun, S. Wu, and A. Men, "Super-resolution time of arrival estimation for a symbiotic FM radio data system," *IEEE Trans. Broadcast.*, vol. 66, no. 4, pp. 847–856, Dec. 2020.

[18] M. Psiaki and B. Slosman, "Tracking digital FM OFDM signals for the determination of navigation observables," *NAVIGATION: J. Inst. Navigat.*, vol. 69, no. 2, pp. 1–35, 2022.

[19] C. Yang and A. Soloviev, "Mobile positioning with signals of opportunity in urban and urban canyon environments," in *Proc. IEEE/ION Position, Location Navigat. Symp. (PLANS)*, Apr. 2020, pp. 1043–1059.

[20] T. Hong, J. Sun, T. Jin, Y. Yi, and J. Qu, "Hybrid positioning with DTMB and LTE signals," in *Proc. Int. Wireless Commun. Mobile Comput. (IWCMC)*, Jun. 2021, pp. 303–307.

[21] Z. Jiao et al., "Carrier phase ranging with DTMB signals for urban pedestrian localization and GNSS aiding," *Remote Sens.*, vol. 15, no. 2, pp. 423–446, 2023.

[22] M. Maaref and Z. Kassas, "Autonomous integrity monitoring for vehicular navigation with cellular signals of opportunity and an IMU," *IEEE Trans. Intell. Transp. Syst.*, vol. 23, no. 6, pp. 5586–5601, Jun. 2022.

[23] P. Wang, Y. Wang, and Y. J. Morton, "Signal tracking algorithm with adaptive multipath mitigation and experimental results for LTE positioning receivers in urban environments," *IEEE Trans. Aerosp. Electron. Syst.*, vol. 58, no. 4, pp. 2779–2795, Aug. 2022.

[24] J. Tian, L. Fangchi, T. Yafei, and L. Dongmei, "Utilization of non-coherent accumulation for LTE TOA estimation in weak LOS signal environments," *EURASIP J. Wireless Commun. Netw.*, vol. 2023, no. 1, pp. 1–31, 2023.

[25] N. Jardak and Q. Jault, "The potential of LEO satellite-based opportunistic navigation for high dynamic applications," *Sensors*, vol. 22, no. 7, pp. 2541–2565, 2022.

[26] C. Zhao, H. Qin, N. Wu, and D. Wang, "Analysis of baseline impact on differential Doppler positioning and performance improvement method for LEO opportunistic navigation," *IEEE Trans. Instrum. Meas.*, vol. 72, pp. 1–10, 2023.

[27] Z. Kassas, S. Kozhaya, J. Saroufim, H. Kanj, and S. Hayek, "A look at the stars: Navigation with multi-constellation LEO satellite signals of opportunity," *Inside GNSS Mag.*, vol. 18, no. 4, pp. 38–47, 2023.

[28] Z. Kassas and A. Abdallah, "No GPS no problem: Exploiting cellular OFDM-based signals for accurate navigation," *IEEE Trans. Aerosp. Electron. Syst.*, vol. 59, no. 6, pp. 9792–9798, Dec. 2023.

[29] A. Abdallah, J. Khalife, and Z. Kassas, "Experimental characterization of received 5G signals carrier-to-noise ratio in indoor and urban environments," in *Proc. IEEE 93rd Veh. Technol. Conf. (VTC-Spring)*, Apr. 2021, pp. 1–5.

[30] R. Whiton, J. Chen, T. Johansson, and F. Tufvesson, "Urban navigation with LTE using a large antenna array and machine learning," in *Proc. IEEE 95th Veh. Technol. Conf. (VTC-Spring)*, Jun. 2022, pp. 1–5.

[31] C. Yang, M. Arizabaleta-Diez, P. Weitkemper, and T. Pany, "An experimental analysis of cyclic and reference signals of 4G LTE for TOA estimation and positioning in mobile fading environments," *IEEE Aerosp. Electron. Syst. Mag.*, vol. 37, no. 9, pp. 16–41, Sep. 2022.

[32] Z. Kassas, M. Maaref, J. Morales, J. Khalife, and K. Shamei, "Robust vehicular localization and map matching in urban environments through IMU, GNSS, and cellular signals," *IEEE Intell. Transp. Syst. Mag.*, vol. 12, no. 3, pp. 36–52, Fall. 2020.

[33] J. Khalife and Z. Kassas, "On the achievability of submeter-accurate UAV navigation with cellular signals exploiting loose network synchronization," *IEEE Trans. Aerosp. Electron. Syst.*, vol. 58, no. 5, pp. 4261–4278, Oct. 2022.

[34] J. del Peral-Rosado et al., "Proof-of-concept of dedicated aerial 5G and GNSS testbed for enhanced hybrid positioning," in *Proc. I_{ON} GNSS Conf.*, Sep. 2022, pp. 2362–2376.

[35] J. Khalife and Z. Kassas, "Differential framework for submeter-accurate vehicular navigation with cellular signals," *IEEE Trans. Intell. Vehicles*, vol. 8, no. 1, pp. 732–744, Jan. 2023.

[36] M. Hameed, M. Philips-Blum, M. Arizabaleta-Diez, and T. Pany, "LTE transmitter states estimation using a combined code and carrier phase observation model," in *Proc. IEEE/ION Position, Location, Navigat. Symp.*, Apr. 2023, pp. 1107–1117.

[37] R. Faragher, C. Sarno, and M. Newman, "Opportunistic radio SLAM for indoor navigation using smartphone sensors," in *Proc. IEEE/ION Position Location Navigat. Symp.*, Apr. 2012, pp. 120–128.

[38] C. Yang and A. Soloviev, "Simultaneous localization and mapping of emitting radio sources–SLAMERS," in *Proc. I_{ON} GNSS Conf.*, Sep. 2015, pp. 2343–2354.

[39] Y. Zeng, X. Xu, S. Jin, and R. Zhang, "Simultaneous navigation and radio mapping for cellular-connected UAV with deep reinforcement learning," *IEEE Trans. Wireless Commun.*, vol. 20, no. 7, pp. 4205–4220, Jul. 2021.

[40] X. Chu et al., "Joint vehicular localization and reflective mapping based on team channel-SLAM," *IEEE Trans. Wireless Commun.*, vol. 21, no. 10, pp. 7957–7974, Oct. 2022.

[41] M. Lotti, G. Pasolini, A. Guerra, F. Guidi, R. D'Errico, and D. Dardari, "Radio SLAM for 6G systems at THz frequencies: Design and experimental validation," *IEEE J. Sel. Topics Signal Process.*, vol. 17, no. 4, pp. 834–849, Jun. 2023.

[42] J. Morales and Z. Kassas, "Tightly coupled inertial navigation system with signals of opportunity aiding," *IEEE Trans. Aerosp. Electron. Syst.*, vol. 57, no. 3, pp. 1930–1948, Jun. 2021.

[43] Z. Kassas and T. Humphreys, "Observability analysis of collaborative opportunistic navigation with pseudorange measurements," *IEEE Trans. Intell. Transp. Syst.*, vol. 15, no. 1, pp. 260–273, Feb. 2014.

[44] Z. Kassas and T. Humphreys, "Receding horizon trajectory optimization in opportunistic navigation environments," *IEEE Trans. Aerosp. Electron. Syst.*, vol. 51, no. 2, pp. 866–877, Apr. 2015.

[45] J. Morales and Z. Kassas, "Stochastic observability and uncertainty characterization in simultaneous receiver and transmitter localization," *IEEE Trans. Aerosp. Electron. Syst.*, vol. 55, no. 2, pp. 1021–1031, Apr. 2019.

[46] Z. Kassas, A. Arapostathis, and T. Humphreys, "Greedy motion planning for simultaneous signal landscape mapping and receiver localization," *IEEE J. Sel. Topics Signal Process.*, vol. 9, no. 2, pp. 247–258, Mar. 2015.

[47] Y. Yang, J. Khalife, J. Morales, and Z. Kassas, "UAV waypoint opportunistic navigation in GNSS-denied environments," *IEEE Trans. Aerosp. Electron. Syst.*, vol. 58, no. 1, pp. 663–678, Feb. 2022.

[48] J. Morales, J. Khalife, and Z. Kassas, "Information fusion strategies for collaborative inertial radio SLAM," *IEEE Trans. Intell. Transp. Syst.*, vol. 23, no. 8, pp. 12935–12952, Aug. 2022.

[49] J. Morales, J. Khalife, and Z. Kassas, "Event-based communication strategies for collaborative inertial radio SLAM," *IEEE Trans. Aerosp. Electron. Syst.*, vol. 59, no. 2, pp. 1624–1642, Apr. 2023.

[50] Z. Kassas, J. Khalife, A. Abdallah, and C. Lee, "I am not afraid of the GPS jammer: Resilient navigation via signals of opportunity in GPS-denied environments," *IEEE Aerosp. Electron. Syst. Mag.*, vol. 37, no. 7, pp. 4–19, Jul. 2022.

[51] J. Honda and T. Otsuyama, "Feasibility study on aircraft positioning by using ISDB-T signal delay," *IEEE Antennas Wireless Propag. Lett.*, vol. 15, pp. 1787–1790, 2016.

[52] B. W. Stevens and M. F. Younis, "Detection algorithm for cellular synchronization signals in airborne applications," *IEEE Access*, vol. 9, pp. 55555–55566, 2021.

[53] Z. Kassas, J. Morales, K. Shamaei, and J. Khalife, "LTE steers UAV," *GPS World Mag.*, vol. 28, no. 4, pp. 18–25, Apr. 2017.

[54] E. Kim and Y. Shin, "Feasibility analysis of LTE-based UAS navigation in deep urban areas and DSRC augmentation," *Sensors*, vol. 19, no. 9, pp. 4192–4207, Apr. 2019.

[55] E. Kim and Y. Shin, "Analysis of the signals of opportunity and cooperative based positioning for UAS navigation in deep urban area," in *Proc. Integr. Commun., Navigat. Surveill. Conf. (ICNS)*, Apr. 2019, pp. 1–8.

[56] J. Mortier, G. Pagès, and J. Vilà-Valls, "Robust TOA-based UAS navigation under model mismatch in GNSS-denied harsh environments," *Remote Sens.*, vol. 12, no. 18, pp. 2928–2947, Sep. 2020.

[57] N. Souli, R. Makrigiorgis, P. Kolios, and G. Ellinas, "Real-time relative positioning system implementation employing signals of opportunity, inertial, and optical flow modalities," in *Proc. Int. Conf. Unmanned Aircr. Syst. (ICUAS)*, Jun. 2021, pp. 229–236.

[58] Z. Kassas et al., "Received power characterization of terrestrial cellular signals on high altitude aircraft," in *Proc. IEEE Aerosp. Conf. (AERO)*, Mar. 2022, pp. 1–8.

[59] Z. Kassas et al., "Assessment of cellular signals of opportunity for high-altitude aircraft navigation," *IEEE Aerosp. Electron. Syst. Mag.*, vol. 37, no. 10, pp. 4–19, Oct. 2022.

[60] Z. Kassas et al., "Flight demonstration of high altitude aircraft navigation with cellular signals," *IEEE Intell. Transp. Syst. Mag.*, vol. 15, no. 4, pp. 150–165, Oct. 2023.

[61] J. Farrell and M. Barth, *The Global Positioning System and Inertial Navigation*. New York, NY, USA: McGraw-Hill, 1998.

[62] P. Groves, *Principles of GNSS, Inertial, and Multisensor Integrated Navigation Systems*, 2nd ed. Norwood, MA, USA: Artech House, 2013.

[63] X. R. Li and V. P. Jilkov, "Survey of maneuvering target tracking. Part I: Dynamic models," *IEEE Trans. Aerosp. Electron. Syst.*, vol. 39, no. 4, pp. 1333–1364, Oct. 2003.

[64] R. Brown and P. Hwang, *Introduction to Random Signals and Applied Kalman Filtering With MATLAB Exercises*, 4th ed. Hoboken, NJ, USA: Wiley, 2012.

[65] A. Thompson, J. Moran, and G. Swenson, *Interferometry and Synthesis in Radio Astronomy*, 2nd ed. Hoboken, NJ, USA: Wiley, 2001.

[66] J. Khalife, K. Shamaei, and Z. Kassas, "Navigation with cellular CDMA signals—Part I: Signal modeling and software-defined receiver design," *IEEE Trans. Signal Process.*, vol. 66, no. 8, pp. 2191–2203, Apr. 2018.

[67] Z. Kassas et al., "Robust receiver design for high altitude aircraft navigation with terrestrial cellular signals," in *Proc. IEEE/ION Position, Location Navigat. Symp. (PLANS)*, Apr. 2023, pp. 75–80.

[68] J. Khalife, M. Maaref, and Z. Kassas, "Opportunistic autonomous integrity monitoring for enhanced UAV safety," *IEEE Aerosp. Electron. Syst. Mag.*, vol. 38, no. 5, pp. 34–44, May 2023.

[69] M. Jia, J. Khalife, and Z. Kassas, "Performance analysis of opportunistic ARAIM for navigation with GNSS signals fused with terrestrial signals of opportunity," *IEEE Trans. Intell. Transp. Syst.*, vol. 24, no. 10, pp. 10587–10602, Oct. 2023.

[70] M. Jia and Z. Kassas, "Fault detection and exclusion for INS/GPS/5G tightly-coupled navigation," in *Proc. IEEE/ION Position, Location Navigat. Symp. (PLANS)*, Apr. 2023, pp. 597–602.

Zaher (Zak) M. Kassas (Fellow, IEEE) received the B.E. degree (Hons.) in electrical engineering from Lebanese American University, the M.S. degree in electrical and computer engineering from The Ohio State University, and the M.S.E. degree in aerospace engineering and the Ph.D. degree in electrical and computer engineering from The University of Texas at Austin. He is currently the TRC Endowed Chair of Intelligent Transportation Systems and a Professor in electrical and computer engineering at The Ohio State University. He is also the Director of the Autonomous Systems Perception, Intelligence, and Navigation (ASPIN) Laboratory as well as the Director of U.S. Department of Transportation Center: Center for Automated Vehicle Research with Multimodal AssuEd Navigation (CARMEN), focusing on navigation resiliency and security of highly automated transportation systems. His research interests include cyber-physical systems, navigation systems, and intelligent transportation systems. He is a fellow of the Institute of Navigation (ION) and a Distinguished Lecturer of the IEEE Aerospace and Electronic Systems Society. He was a recipient of the National Science Foundation (NSF) CAREER Award, Office of Naval Research (ONR) Young Investigator Program (YIP) Award, Air Force Office of Scientific Research (AFOSR) YIP Award, IEEE Walter Fried Award, ION Samuel Burka Award, ION Colonel Thomas Thurlow Award, and IEEE Harry Rowe Mimno Award. He is a Senior Editor of IEEE TRANSACTIONS ON INTELLIGENT TRANSPORTATION SYSTEMS and an Associate Editor of IEEE TRANSACTIONS ON AEROSPACE AND ELECTRONIC SYSTEMS.

Nadim Khairallah received the B.E. degree (Hons.) in mechanical engineering from American University of Beirut and the M.S. degree in mechanical and aerospace engineering from the University of California at Irvine. His research interests include satellite-based opportunistic navigation, sensor fusion, and estimation theory. He was a member of the ASPIN Laboratory. He was a recipient of the 2022 U.S. Department of Transportation Graduate Student of the Year Award and 2022 IEEE Vehicular Technology Conference Best Student Paper Award.

Joe J. Khalife (Member, IEEE) received the B.E. degree in electrical engineering and the M.S. degree in computer engineering from Lebanese American University and the Ph.D. degree in electrical engineering and computer science from the University of California at Irvine. He was a Post-Doctoral Fellow with the University of California at Irvine and a member of the ASPIN Laboratory. He was a recipient of 2016 IEEE/ION Position, Location, and Navigation Symposium (PLANS) Best Student Paper Award, 2018 IEEE Walter Fried Award, and 2021 IEEE AESS Robert T. Hill Best Dissertation Award.

Chiawei Lee received the B.S. degree in aerospace engineering from the University of California at Los Angeles and the M.S. degree in aero/astro engineering from Stanford University. He is currently an Assistant Professor and an Instructor Flight Test Engineer with U.S. Air Force Test Pilot School. He is also the Test Management Program Director, where he oversees about a dozen student and staff led flight test projects each year. In addition, he is the Chief Test Safety Officer responsible for the safe execution of curriculum and flight test project safety packages.

Juan Jurado (Member, IEEE) received the B.S. degree from Texas A&M University, the M.S. degree from the Air Force Test Pilot School, and the M.S. and Ph.D. degrees from the Air Force Institute of Technology. He is currently a U.S. Air Force Lieutenant Colonel and the Director of Education with U.S. Air Force Test Pilot School. Previously, he was the Director of Engineering with the 413th Flight Test Squadron and oversaw various C-130, V-22, and H-1 flight test programs. His research interests include aircraft performance modeling, online sensor calibration, image processing, and multi-sensor navigation.

Steven Wachtel received the B.S. degree in mechanical engineering from The Ohio State University, the M.S. degree in flight test engineering from U.S. Air Force Test Pilot School, and the M.S. degree in systems engineering from the Air Force Institute of Technology. He is currently a U.S. Air Force Captian and a Flight Test Engineer, assigned to the 780th Test Squadron, Eglin AFB, FL, USA.

Jacob Duede received the B.S. degree in mechanical engineering from U.S. Air Force Academy, the degree from U.S. Air Force Test Pilot School, Edwards Air Force Base, CA, USA, the M.S. degree in engineering from the University of Arkansas, and the M.S. degree in flight test engineering from Air University. He is currently a Major with U.S. Air Force. He was trained as a Communication/Navigation/Mission Systems Apprentice on C-17 Globmaster II aircraft. He is also a Senior Pilot with over 2 000 hours.

Zachary Hoeffner received the B.S. degree in nuclear engineering from U.S. Air Force Academy, the M.S. degree in flight test engineering from U.S. Air Force Test Pilot School, the M.S. degree in physics engineering and in applied physics and the M.S. degree in nuclear engineering from the Air Force Institute of Technology. He is currently a Flight Test Engineer with U.S. Air Force.

Thomas Hulsey received the B.S. degree in aerospace engineering from Missouri University of Science and Technology, the M.S. degree in aeronautical engineering from the Air Force Institute of Technology, and the M.S. degree in experimental flight test engineering from the United States Air Force Test Pilot School. He is currently a U.S. Air Force Flight Commander in operations engineering.

Rachel Quirarte received the B.S. degree in aeronautical engineering from U.S. Air Force Academy, the M.S. degree in flight test engineering from U.S. Air Force Test Pilot School, and the M.S. degree in mechanical engineering from Rice University. She is currently a KC-46 and KC-135 Programmatic Flight Commander and a Test Pilot with the 418th Flight Test Squadron, U.S. Air Force.

RunXuan Tay received the B.S. degree in electrical engineering from the University California at San Diego and the M.S. degree in flight test engineering from U.S. Air Force Test Pilot School. He is currently a Test Pilot with the Air Warfare Center, Republic of Singapore Air Force, where he works on fixed wing test programs.